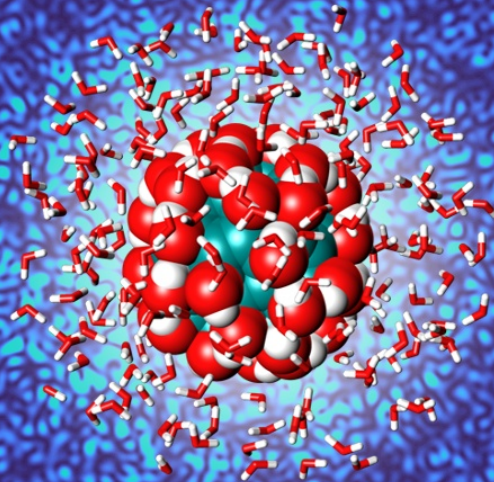# The Role of Molecular Heterogeneity in the Structural Dynamics of Aqueous Solutions

Sharon Berkowicz

The Role of Molecular Heterogeneity in the Structural Dynamics of Aqueous Solutions

Sharon Berkowicz

Abstract

The liquid-liquid critical point hypothesis suggests that liquid water exists in two liquid states with different local structures, so-called high- and low-density liquid (HDL, LDL). At ambient pressure water locally fluctuates between these two states, with the fluctuations becoming more pronounced as the liquid is supercooled. In this thesis, we explore the role of molecular heterogeneity in the structural dynamics of aqueous solutions, specifically investigating the interplay of different solutes in water with the hypothesized HDL-LDL fluctuations. In our experimental approach, we utilize coherent light and X-ray scattering techniques, including small- and wide-angle X-ray scattering (SAXS, WAXS), as well as correlation methods, such as dynamic light scattering (DLS) and X-ray photon correlation spectroscopy (XPCS), that enable us to probe structural dynamics at a broad range of length and time scales.

Using DLS, we measure the diffusive dynamic behaviour of differently sized nanomolecular probes in supercooled water, finding that it is effectively similar and independent of probe size down to molecular scales of $\approx$1 nm. In contrast to single water molecules, these probes experience a similar dynamic environment, which coincides with the bulk viscosity. These results could suggest that anomalous influence from the hypothesized water fluctuations becomes apparent first on sub-nm length scales. Furthermore, we explore how the presence of small polar-organic solutes modulates the water phase diagram, utilizing glycerol-water solutions as a model system. By outrunning freezing with the rapid evaporative cooling technique, combined with ultrafast X-ray scattering at X-ray free-electron lasers (XFELs), we are able to probe the liquid structure in deeply supercooled dilute glycerol-water solutions. Our findings indicate the existence of HDL- and LDL-like fluctuations upon supercooling, with a Widom line shifted to slightly lower temperatures compared to pure water. Further experiments on deeply supercooled glycerol-water solutions at intermediate glycerol concentrations, combining WAXS and SAXS/XPCS, provide additional insights. These results reveal a first-order-like liquid-liquid transition involving discontinuous changes in the inter-atomic liquid structure and nanoscale liquid dynamics, which precedes ice crystallization.

Lastly, with the aim of developing powerful tools for resolving dynamics within spatially heterogeneous systems, including aqueous solutions, we combine the spatial resolution of nanofocused coherent X-ray beams with dynamic measurements by XPCS. Here, we successfully demonstrate a first proof-of-concept experiment of so-called nanofocused XPCS at MAX IV synchrotron radiation facility. In future experiments, we plan to go beyond standard XPCS at synchrotrons, towards accessing ultrafast atomic-scale liquid dynamics by X-ray speckle visibility spectroscopy (XSVS) at XFELs.

Department of Physics

Stockholm University, 106 91 Stockholm

THE ROLE OF MOLECULAR HETEROGENEITY IN THE
STRUCTURAL DYNAMICS OF AQUEOUS SOLUTIONS

Sharon Berkowicz

The Role of Molecular Heterogeneity in the Structural Dynamics of Aqueous Solutions

Sharon Berkowicz

To my beloved family

Am Yisrael Chai

Contents

List of Papers

This thesis includes the following papers. Reprints were made with permission from the publishers.

PAPER I: **Exploring the Validity of the Stokes-Einstein Relation in Supercooled Water using Nanomolecular Probes**
S. Berkowicz and F. Perakis.
Phys. Chem. Chem. Phys., **23**, 25490 (2021).
DOI: 10.1039/d1cp02866a.

PAPER II: **Nanofocused X-ray Photon Correlation Spectroscopy**
S. Berkowicz, S. Das, M. Reiser, M. Filianina, M. Bin, G. Crevatin, F. Hennies, C. Weninger, A. Björling, P. Bell and F. Perakis.
Phys. Rev. Res., 4, L032012 (2022).
DOI: 10.1103/PhysRevResearch.4.L032012

PAPER III: **Resolving Nanoscale Dynamics during a Liquid-Liquid Transition in Supercooled Glycerol-Water Solutions**
S. Berkowicz, M. Filianina, M. Bin, R. Tyburski, A. Girelli, R. Bauer, F. Zontone, Y. Chushkin, M. Sprung, F. Westermeier, W. Roseker, F. Lehmkühler and F. Perakis.
Manuscript in preparation (2023).

PAPER IV: **Unveiling the Structure and Thermodynamics of Deeply Supercooled Glycerol-Water Microdroplets with Ultrafast X-ray Scattering**
S. Berkowicz, I. Andronis, M. Filianina, M. Bin, A. Girelli, K. Nam, M. Shin, M. Kowalewski, T. Katayama, K. H. Kim, A. Nilsson and F. Perakis.
Manuscript in preparation (2023).

The following are papers to which I have contributed, but which are not part of the main thesis work and therefore not included in this thesis.

PAPER V: **Wide-angle X-ray Scattering and Molecular Dynamics Simulations of Supercooled Protein Hydration Water**

M. Bin, R. Yousif, <u>S. Berkowicz</u>, S. Das, D. Schlesinger and F. Perakis.
Phys. Chem. Chem. Phys., **23**, 18308 (2021).
DOI: 10.1039/d1cp02126e.

PAPER VI: **Resolving Molecular Diffusion and Aggregation of Antibody Proteins with Megahertz X-ray Free-Electron Laser Pulses**
M. Reiser, A. Girelli, A. Ragulskaya, S. Das, <u>S. Berkowicz</u>, M. Bin, M. Ladd-Parada, H-F. Poggemann, N. Begam, M. S. Akhundzadeh, S. Timmermann, L. Randolph, Y. Chushkin, T. Seydel, U. Bösenberg, J. Hallmann, J. Möller, A. Rodriguez-Fernandez, R. Rosca, R. Schaffer, M. Scholz, R. Shayduk, Alexey Zozulya, A. Madsen, F. Schreiber , F. Zhang, F. Perakis and C. Gutt.
Nat. Commun., **13**, 5528 (2022).
DOI: 10.1038/s41467-022-33154-7

PAPER VII: **Coherent X-ray Scattering Reveals Nanoscale Fluctuations in Hydrated Proteins**
M. Bin, M. Reiser, M. Filianina, <u>S. Berkowicz</u>, S. Das, S. Timmermann, W. Roseker, R. Bauer, J. Öström, A. Karina, K. Amann-Winkel, Ma. Ladd-Parada, F. Westermeier, M. Sprung, J. Möller, F. Lehmkühler, C. Gutt, and F. Perakis.
J. Phys. Chem. B, **127**, 21, 4922 (2023).
DOI: 10.1021/acs.jpcb.3c02492.

PAPER VIII: **Nanocrystallites Modulate Intermolecular Interactions in Cryoprotected Protein Solutions**
M. Filianina, M. Bin, <u>S. Berkowicz</u>, M. Reiser, H. Li, S. Timmermann, M. Blankenburg, K. Amann-Winkel, C. Gutt, and F. Perakis.
J. Phys. Chem. B, **127**, 27, 6197 (2023).
DOI: 10.1021/acs.jpcb.3c02413.

PAPER IX: **Resolving Hydrodynamic Function of Protein in Crowded Solutions Through Coherent X-Ray Scattering with XFELs**
A. Girelli, M. Filianina, M. Bin, S. Timmermann, <u>S. Berkowicz</u>, M. Reiser, S. Retzbach, M. Senft, M. Kowalski, M. Dargasz, N. Das, M. Sayed Akhundzadeh, Y. Chushkin, T. Seydel, J. Hallmann, J. Möller, A. Rodriguez-Fernandez, J.-E. Pudell, F. Brausse, W. Lu, W. Jo, R. Shayduk, A. Zozulya, A. Madsen, M. Paulus, F. Schreiber, F. Zhang, C. Gutt, and Fivos Perakis.
Manuscript in preparation (2023).

Author's Contributions

My contributions in this thesis can be summarized as follows:

Paper I: Using dynamic light scattering (DLS), we investigated the diffusive dynamics of nanomolecular probes in water as a function of temperature and probe size, utilizing simple model solutes in the form of spherical silica nanoparticles as well as molecular-sized polyhydroxylated fullerenes (≈ 1 nm). I solely designed the experimental protocol, including the choice of sample system, and performed the sample preparation, DLS measurements as well as data analysis, with guidance from the supervisor. In addition, I wrote the resulting paper independently, with feedback and discussions with the supervisor.

Paper II: In a novel prototype X-ray photon correlation spectroscopy (XPCS) experiment performed at the NanoMAX beamline, at the MAX IV synchrotron radiation facility, we evaluated the use of nanofocused X-ray beams for extracting structural dynamic information. The XPCS experiment itself, as usual a team effort, was conducted practically onsite by the beamline staff with remote online participation from the rest of the team due to the Covid-19 pandemic. Nevertheless, I was active in the planning of the experiment, prepared and precharacterised the samples (nanoparticle suspensions) with DLS, contributed to the decision-making and online data analysis. Additionally, I performed the post-beamtime data analysis and, together with feedback from my supervisor (F. Perakis), finally wrote the resulting paper. The disentanglement of nanobeam-induced effects from sample dynamics, and the development of the analysis model to account for these effects, constituted the major challenges in the data analysis and data interpretation.

Paper III: This manuscript builds on results from synchrotron radiation experiments at facilities DESY (P10 beamline) and ESRF (ID10 beamline) conducted in September-October 2022, for which I was the main proposer. In these experiments, we measured the changes in the liquid structure and dynamics in intermediate-composition glycerol-water solutions following quenching to cryogenic temperatures, using a combination of wide-angle X-ray scattering (WAXS), small-angle X-ray scattering (SAXS) and XPCS. The aim was

to capture a possible liquid-liquid transition hypothesized in this deeply super-cooled regime. I performed the preliminary tests with table-top X-ray diffraction (XRD) at Stockholm university, prepared the sample solutions, designed the experiments and led the team efforts on-site. In addition, I conducted the post-beamtime analysis of the collected experimental data (still in progress) and, in collaboration with my supervisor (F. Perakis), I wrote the manuscript.

Paper IV: Here, we utilized rapid evaporative cooling and ultrafast SAXS and WAXS to probe liquid structural changes and density fluctuations in deeply supercooled dilute glycerol-water solutions. The experiment was conducted at the X-ray free-electron laser (XFEL) SACLA in Japan (November 2022) by an international team from Stockholm University and POSTEC (South Korea), led by me as the main proposer. With guidance from my supervisor (F. Perakis), I designed the experiment, wrote the beamtime proposal, tested and tuned the experimental setup, handled transport logistics of large experimental equipment to Japan and led the experiment on-site. I also performed the post-beamtime analysis of the experimental data and wrote the paper manuscript, in collaboration with F. Perakis (supervisor) and Iason Andronis (PhD student), who conducted the complementary molecular dynamics (MD) simulations.

Additional contributions
Here, I list my additional contributions, which are still at an early stage and not yet resulted in a manuscript, or not included in the main thesis work.

Designing experiments at X-ray facilities: A considerable part of the work done in the field of coherent X-ray scattering relates to applying for beamtime at synchrotron radiation and XFEL facilities around the world. This includes designing the experiments, from choosing the appropriate experimental configuration, in order to answer the research questions, to estimating the feasibility of the experiment, as well as writing the beamtime proposals. I have been active and one of the main responsible in designing and writing several proposals that directly connect to this thesis work. These include beamtime proposals to XFELs, whereof five proposals to Linac Coherent Light source (LCLS), one proposal to SACLA XFEL, one to the Swiss free-electron laser (SwissFEL), and to synchrotron radiation facilities, including one proposal each at MAX IV, ESRF and DESY. Out of these, four proposals for which I was the main proposer were allocated beamtime (LCLS, SACLA, ESRF and DESY).

Experimental investigations of spatial heterogeneities in model liquid mixtures and development of X-ray speckle visibility spectroscopy (XSVS): A currently early-stage research project focused on increasing our fundamental understanding of liquid-liquid phase separation by studying model systems of aqueous liquid mixtures, in particular aqueous mixtures of Dimethyl sulfoxide (DMSO). I have conducted preliminary experiments on these systems in-house using DLS and XRD, as well as SAXS with synchrotron radiation (DESY, P21 beamline). Additionally, I have designed an XFEL experiment proposal in collaboration with my supervisor (F. Perakis), for which I am the spokesperson, that has been allocated beamtime at the XFEL LCLS in the US in November 2023 (postponed from March 2023 due to a facility incident which required a shutdown of all operations). The aim of this experiment is to capture the picosecond time scale intermediate scattering function of DMSO-water solutions with XSVS. As much as the project is motivated by phenomenological scientific interest to understand heterogeneous dynamics on the atomic-scale, it is an strategic step in the method-development of XSVS that has not yet been successfully demonstrated experimentally. Earlier attempts of XSVS on pure water has suffered from poor signal-to-noise or insufficient pulse-pair overlap due to angular mismatch. In the current experiment, however, the use of DMSO is predicted to contribute to increased signal-to-noise, by stronger scattering intensity at lower momentum transfer q, and the angular mismatch can be overcome by utilizing the state-of-the-art split-and-delay unit at LCLS, that generate XFEL pulse pairs with picosecond separation by amplitude splitting.

Design and development of a cryogenic DLS setup: Here, the aim is to build a customized lab-based DLS setup for measuring dynamics in supercooled cryoprotectant solutions at cryogenic temperatures. I have been actively involved in creating the optical design and procurement of the optical components, as well as in building and preliminary testing the setup at ambient conditions. The remaining step in the development involves integration of a cryostat, i.e. the sample environment to enable cryogenic cooling, followed by further optimization, e.g. laser alignment, and test measurements on cryo-cooled samples.

Beamtime participation (team projects)*:** Experiments performed at synchrotrons and XFELs are usually team efforts. Part of the work within the research group therefore involves participating in synchrotron and XFEL experiments and contributing to related research projects within the group. These include experiments at the European XFEL (MID station), ESRF (ID2 beamline) and DESY (P10 and P21 beamlines), which have so far resulted in paper V-X where I am co-author. Most of these are not part of my main thesis work and therefore not included in this thesis.

Paper V*: Here, my contributions relate to active participation in the XRD experiments that form the experimental basis of the study, as well as in group discussions on data interpretation.

Paper VI-X*: I contributed as part of the experiment team performing the experiments at the synchrotron radiation or XFEL facility, and participated in the following discussions about the analysis and interpretation of the results.

* Not part of the main thesis work and therefore not included in this thesis.

Author's Notes

This thesis is a continuation of my licentiate thesis. Therefore, some content (text, tables and figures) from the licentiate thesis has been reused herein, in its original form or partially edited as appropriate.

Abbreviations

DLS	Dynamic light scattering
DMSO	Dimethyl sulfoxide
HDA	High-density amorphous ice
HDL	High-density liquid
KWW	Kohlrausch-Williams-Watts
LDA	Low-density amorphous ice
LDL	Low-density liquid
LLCL	Liquid-liquid critical line
LLCP	Liquid-liquid critical point
LLT	Liquid-liquid transition
LRO	Long-range order
MD	Molecular dynamics
MSD	Mean-squared displacemet
PDT	Protein dynamic transition
PHF	Polyhydroxylated fullerene
SAXS	Small-angle X-ray scattering
SE	Stokes-Einstein
SNR	Signal-to-noise
SRO	Short-range order
TTC	Two-time correlation
USAXS	Ultra small-angle X-ray scattering
WAXS	Wide-angle X-ray scattering
XFEL	X-ray free-electron laser
XPCS	X-ray photon correlation spectroscopy
XSVS	X-ray speckle visibility spectroscopy

1. Introduction

Aqueous solutions are found abundantly in nature, existing as mixtures of water and solutes in various concentrations and conditions. These solutions often exhibit intricate and non-ideal solution behaviors arising from the delicate balance between intermolecular forces, contributing to the enthalpy, and mixing entropy [1–3]. In an ideal solution, similar interaction strengths between its components results in zero mixing enthalpy. The Gibbs free energy of mixing in this case is solely determined by the mixing entropy, the maximization of which favors a uniform mixture (see Fig. 1.1A). Thus, ideal solutions are completely miscible regardless of their composition [4]. In contrast, real aqueous solutions, such as that of polar-organic molecules, encompass a wide array of intermolecular interactions, both hydrophilic and hydrophobic in nature. These fluid systems are characterized by dynamic structures or domains formed through locally favored interactions, constantly fluctuating in space [1–3]. As depicted in Fig. 1.1C, the formation of these transient clusters (see Fig. 1.1B) gives rise to microscopic spatial heterogeneities or liquid-liquid phase separation, a structural dynamic phenomenon which may play a key role in driving important dynamic, self-assembly processes in natural aqueous systems, including vital biological processes such as intracellular organization, biochemical reactions, and cell signaling [5].

Notably, spatial heterogeneities are believed to play a significant role in pure liquid water as well. As described in chapter 2, water possesses many anomalous liquid properties, making it an atypical solvent [6]. With support from recent experimental evidence and theoretical simulations, it is hypothesized that under ambient pressure, liquid water is, in reality, a fluctuating mixture of two distinct liquid states. These fluctuations become more pronounced as water is supercooled below the freezing point while remaining in the liquid state [7–12]. Hence, water itself exhibits spatial heterogeneities (Fig. 1.1C, case I). Although the two phases in this case both consist of water molecules, the transient local arrangements of water molecules differ, resulting in distinct local density, structure and dynamics [7–12].

Despite the intriguing presence of spatial heterogeneities in both pure water and aqueous solutions, their physical nature and underlying mechanisms remain largely unexplored. Specifically, the relationship between these heterogeneities and complex solution dynamics remains unclear [1]. Furthermore,
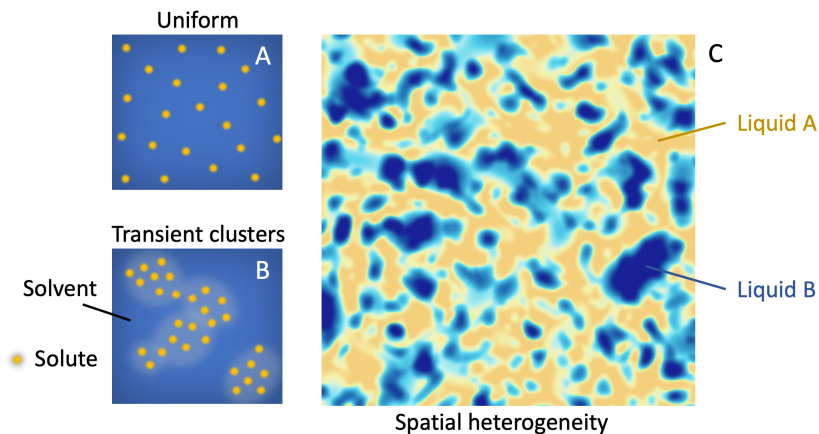
Figure 1.1: Schematics of spatial heterogeneities in liquids. (A) A uniform random distribution of solutes dissolved in a solvent, while in (B) various intermolecular interactions result in the formation of transient clusters, giving rise to a microscopic liquid-liquid phase separation and a spatially heterogeneous liquid. (C) A schematic snapshot of a spatially heterogeneous liquid mixture of liquid A and B. Here, there are two distinct cases: Case I. $A \leftrightarrow B$, liquids A and B have the same chemical composition but different local structure and/or dynamics. This is for instance the hypothesized scenario for pure liquid water. Case II. $A \nleftrightarrow B$, liquids A and B have different chemical compositions and form transient domains similar to what is shown in B. This latter case may for example apply to various aqueous-organic solutions.

we have yet to understand how intrinsic spatial heterogeneities in water could interact with or impact solute dynamics in aqueous solutions [13–15]. If this interplay exists, it suggests that water could have a more active function in biological and other natural systems than we have previously comprehended. While the influence of water fluctuations may be subtle at ambient temperatures, it could become more significant in supercooled aqueous solutions. For example, this is relevant for climate systems and in medicine for biological cryopreservation. The latter utilizes aqueous cryoprotectant solutions that often consist of mixtures of water and small polar-organic molecules, such as glycerol, which suppress ice crystallization to prevent damage to the biological material. Consequently, gaining a deeper fundamental understanding of heterogeneities in aqueous solutions holds tremendous potential across a wide range of applications.

Within the scope of this thesis, we set to experimentally explore the role and character of spatial heterogeneities in the structural dynamics of aqueous solutions. In our experimental approach, we employ coherent light and X-ray scattering techniques, including (static) small- and wide-angle X-ray scattering

(SAXS, WAXS), which can resolve the nano- to atomic scale structures, as well as correlation methods such as dynamic light scattering (DLS) and X-ray photon correlation spectroscopy (XPCS). The latter techniques enable us to probe structural dynamics at length scales ranging from micrometers to atomic distances. The thesis work encompasses two primary aims:

1. Investigating the nano- to atomic scale structure and dynamics of aqueous solutions, focusing on solutions of water and simple model solutes (nanoparticles and small polar-organic cryoprotectant molecules) under both ambient and supercooled conditions. Here, the aim is to increase our understanding of the structural and dynamical character of hypothesized water fluctuations and the interplay between these fluctuations and different solutes (*Paper I*, *III* and *IV*).

2. Developing X-ray photon correlation spectroscopy as a powerful tool for studying dynamics within spatially heterogeneous systems (*Paper II*).

2. Supercooled Aqueous Solutions

2.1 Water and the Liquid-Liquid Critical Point Hypothesis

Water is the most ubiquitous liquid on Earth, and indispensable for most aspects of our lives. As we search for the existence of life in other parts of the universe, we first look for the presence of liquid water, the solvent in which all living processes take place and, as such, the most fundamental component for biological life as we know it. While the water molecule on its own is simple – an oxygen atom covalently bonded to two hydrogen atoms – the structure and dynamics of a crowd of water molecules in liquid water turns out to be very complex. As we shall see, this complexity, and many of the unusual properties of water, can be traced back to the water molecule's ability to form up to four, highly directional hydrogen bonds, enabling the formation of extensive three dimensional hydrogen-bond networks [8].

The properties of water have wide implications in nature. Ambient liquid water has remarkably high heat capacity and surface tension, while low compressibility [8, 16]. The former allows water to serve as heat reservoir and sea water streams to transport heat between continents, both of which have huge impact on the Earth's climate. Amongst water's many anomalous features, the density maximum of the liquid at $T = 277$ K is perhaps one of the most striking [6, 8]. Unlike typical liquids, such as alcohols and hydrocarbons, for which the density linearly increases upon cooling, the density of liquid water decreases below $T = 277$ K (see Fig. 2.1), meaning that the liquid structure expands when cooled, until it crystallizes with an even more open (hexagonal ice) structure. This unusual trend is the reason why ice floats on water and, for example, prevents bottom-freezing of lakes and oceans, while the frozen top layer allows to reflect sunlight and heat away from the Earth's surface. Other properties, such as the formerly mentioned (isobaric) heat capacity C_p and (isothermal) compressibility κ_T, also exhibit similar anomalous behaviours but with minima at 308 K (35°C) and 320 K (46.5°C), respectively (see Fig. 2.1), meaning that water behaves as an anomalous liquid even at tem-

peratures associated with biological activity [6, 8].

As liquid water is cooled below its freezing point ($T = 273$ K at ambient pressure), entering the so-called *supercooled* regime where it remains in the liquid state, the anomalous properties become increasingly pronounced. This is evidenced by looking at thermodynamic response functions, which are quantities that describe how a system reacts to external parameters such as temperature and pressure, including isobaric heat capacity and the isothermal compressibility. In particular, these thermodynamic response functions diverge upon supercooling at ambient pressure (see Fig. 2.1) [6]. Moreover, when fitted to a power law equation, associated with mode-coupling theory, these thermodynamic properties all diverge at a similar singular temperature $T_s \approx 230$ K [18]. This temperature is noticeably well-above the glass-transition temperature ($T_g \approx 136$ K) [6, 19] wherefore the question of its origin, as well as that of other water anomalies, has long been the subject of intense debate. In recent years, however, a more comprehensive picture has emerged supported by new experimental evidence [9–12].

Figure 2.1: Anomalous properties of liquid water. The anomalous temperature dependence of density ρ, isobaric heat capacity C_p and isothermal compressibility κ_T that exhibit a maximum and minima, respectively. Based on data given in Ref. [17].

Supercooled water is a metastable state, while ice is the thermodynamically most stable, i.e. it has the lowest Gibbs free energy. Historically, experimental measurements in the supercooled regime have therefore been a technical race against the increasing rate of homogeneous ice nucleation with decreasing temperature. Homogeneous ice nucleation is the spontaneous formation of ice nuclei in the pure liquid [6, 20, 21], which is different from most water crystallization in nature, where impurities such as solid particles catalyze the formation of ice nuclei, so-called heterogeneous ice nucleation. Since conventional cooling methods has been limited to temperatures above the homogeneous ice nucleation temperature $T_H \approx 235$ K (at ambient pressure), i.e. the stability limit against crystallization, the temperature range below T_H has often been referred to as the *"No-man's land"* (see Fig. 2.2) [8]. However, developments of new cooling techniques, most notably rapid evaporative cooling combined with ultrafast probing, have recently allowed to push the limit and enabled experimental investigations of previously unexplored phase-territories
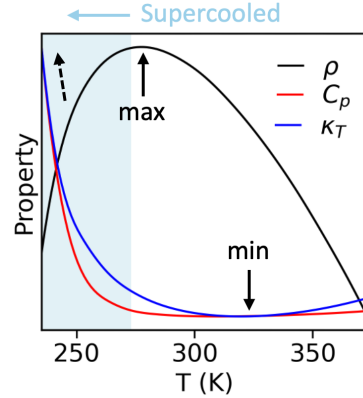
of water [9, 21]. X-ray scattering experiments, utilizing ultrashort intense X-ray laser pulses to probe evaporatively supercooled microdroplets of pure water, have enabled access to temperatures down to $T \approx 227$ K, indicating the presence of a maximum for thermodynamic properties C_p, κ_T as well as for the correlation length ξ at around 229 K [9, 11]. These and other experiments [10, 12], including molecular dynamics (MD) simulations [22–24], support the so-called *liquid-liquid critical point (LLCP) hypothesis* [16] which suggests that water exists as two distinct liquid states with different local structure, so-called *high-density liquid (HDL)* and *low-density liquid (LDL)*. As their names indicate, HDL is more densely packed compared to LDL, that locally has a more open tetrahedral structure similar to hexagonal ice. The dense structure of HDL arises partially from occupation of interstitial sites in the tetrahedral hydrogen-bond network, which in addition introduces more disorder [8]. The idea that there may exist two liquid phases hidden in the No-man's land, was initially sparked by the observation of two glassy states of water, high-density (HDA) and low-density amorphous ice (LDA) [25, 26]. In fact, starting from these glassy states and heating up has proven to be yet another successful approach to experimentally access the deeply supercooled regime [10, 12].

According to the LLCP scenario, the two liquid states of water are separated by a phase-coexistence line which ends in a critical point (see Fig. 2.2), above which the liquids exist as an inseparable fluctuating liquid mixture [8]. The *Widom line* [27], serving as an extension of the LLCP (see Fig. 2.2, grey dashed line), marks the pressure-temperature locations where the HDL-LDL density fluctuations locally maximize, accompanied by local maxima in correlation length and other properties aforementioned [9, 11]. The HDL-LDL fluctuations eventually reach the global maximum at the LLCP where they extend to macroscopic length scales. Upon passing the Widom line, from warm to cold, the heterogeneous liquid mixture undergoes a continuous shift from being an HDL-dominated liquid, with small transient patches of LDL, to an LDL-dominated liquid, as illustrated in Fig. 2.2 (grey-shaded area). Thus, far away from the Widom line liquid water behaves as a normal, single-component liquid, whilst the growth of HDL-LDL fluctuations closer to the Widom line results in anomalous liquid behaviour [8]. Although the exact location of the critical point remains yet to be experimentally confirmed, the observation of the Widom line at $T \approx 229$ K and ambient pressure [9], and the more recent experimental indication of a first-order HDL-LDL *liquid-liquid transition (LLT)* at $T \approx 205$ K between ambient and 3.5 kbar [10], indicates that the LLCP is likely located somewhere between these temperatures (205–229 K) at slightly elevated pressures. Based on comparison between experiments and simulations, it has been estimated that *"the LLCP could be found at ≈ 500 bar and ≈ 223 K"* [28]. This LLCP location, and the fact that water's anomalies ex-
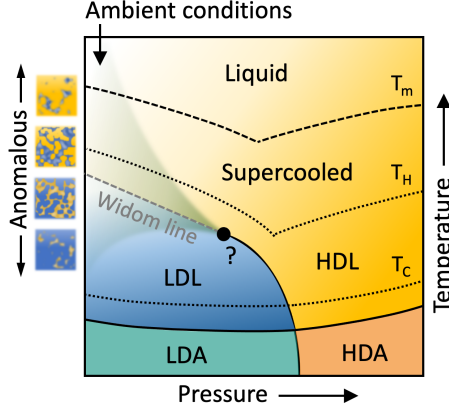
Figure 2.2: The heterogeneous nature of water. A schematic temperature-pressure (T-P) phase diagram of water according to the liquid-liquid critical point (LLCP) hypothesis, in which liquid water exists in two liquid states with different local structure. At elevated pressures, the so-called high-density and low-density liquid states (HDL and LDL) are separated by a phase coexistence line (vertical solid line) that ends in a LLCP (black dot). The dashed grey line that emanates from the LLCP denotes the Widom line and the shadowed area indicates the anomalous T-P region where water exists a fluctuating mixture of HDL and LDL. Dotted black lines denote the upper and lower limit of stability against ice crystallization (encompassing "No-man's land"), the upper black dashed line is the melting temperature while the lower solid black horizontal line indicate the glass transition temperature to low- and high-density amorphous ice (LDA, HDA).

tend to warm temperatures, suggest that liquid water is indeed a heterogeneous mixture even at ambient conditions [8, 10].

There is increasing evidence that the LLCP scenario, with ambient liquid water described as a heterogeneous liquid mixture, can also explain various dynamic phenomena in water. One such phenomenon is an observed dynamic crossover in supercooled water, generally known as the *fragile-to-strong transition* [7, 29, 30]. The classification of liquids as strong or fragile refers to whether or not dynamic properties X_D, such as viscosity and diffusion coefficients, follow an Arrhenius temperature dependence with a single activation energy E_A [7]:

$$X_D(T) \propto \exp\left(-E_A/k_B T\right), \qquad (2.1)$$

where k_B is the Boltzmann constant and T is the temperature. Supercooled water transitions from what appears to be a fragile liquid at ambient temperature to a very strong liquid at low temperature. As it turns out, the fragile-to-strong transition occurs in the vicinity of the Widom line, at around $T \approx 220$ K, which

has led to the hypothesis that the transition could reflect the conversion of the HDL-LDL mixture (fragile) to the LDL-dominated liquid (strong) at low temperature [30]. A related dynamic anomaly is the strong decoupling of the self-diffusion coefficient D of water and viscosity η upon supercooling, causing violation of the *Stokes-Einstein (SE) relation* [31, 32]:

$$D \propto T/\eta \tag{2.2}$$

In particular, water molecules appear to diffuse faster than what the SE relation predicts. The phenomenon has been attributed to dynamical heterogeneities [33], in particular cage effects and activated motion. According to this interpretation, the water molecules move from one caged position to another by coordinated rearrangements through large angular jumps, resulting in a so-called "jump-diffusive motion" rather than small-step diffusion (see also Fig. 3.6 in section 3.2.3) [34–36]. Such effects are expected to become more pronounced in the supercooled regime, along with an increasing fraction of the more rigid tetrahedral hydrogen-bond network of LDL [23, 36, 37].

2.2 Aqueous Solutions

2.2.1 Water as a solvent

Water is a unique solvent in many ways. Because the water molecule is highly polar, liquid water is excellent at solvating polar and ionic compounds, while being a very poor solvent for nonpolar solutes [38]. This combination of hydrophilic and hydrophobic interactions is key in driving vital self-assembly processes of macromolecular structures, from the formation of micelles and membranes [39, 40] to protein folding [41, 42]. Furthermore, water is a weak nucleophile, an H-donor as well as H-acceptor, and can both act as an acid and a base. As such, water molecules often take active part in various chemical reactions, for instance in hydrolysis reactions and by mediating protons in proton transfer reactions, both of which are widely important in biochemical reactions [43, 44] as well as in industrial chemical synthesis [38].

The structure and dynamics of water is often altered in the presence of solutes. These perturbations are most pronounced in the hydration water (i.e. the first few water layers around a solute). The perturbation of the water structure depends widely on the properties of the solute, such as its size, shape, charge, polarity and hydrogen-bonding capability. For instance, some solutes, in particular ions, promote more tetrahedral structures ("structure makers") while others introduce more disorder in the hydrogen-bond network ("structure breakers") [45, 46]. The strong electrostatic field exerted by ions have additionally been observed to induce long-range correlations in the water structure

that reach far beyond the first hydration shell [47]. Other properties like the size and shape can affect how readily a solute can be accommodated in the water network. A solute small enough to fit within the water cages, such as small gas molecules, can leave the hydrogen-bond network almost intact, compared to a highly disrupting big bulky molecule, such as sugars like trehalose [48–50]. The former could explain the increasing gas solubility with decreasing temperature, since it is coupled with a larger fraction LDL associated with a higher degree of tetrahedrality [49]. Furthermore, there is evidence that the impact of the solute's structure on the water can even go as far as solute-imposed chirality, for instance in the form of hydration water superstructures around chiral biomolecules such as the DNA helix [51, 52].

In contrast to non-interacting nonpolar species such as hydrocarbons, polar solutes with the ability to form hydrogen bonds (i.e. polar protic solutes) can actively participate in the water network. Since many solutes contain both non-polar and polar moieties, there can be competing interactions, and the resulting effect on the water structure can therefore be quite complex [53, 54]. For example, studies indicate that small alcohols such as methanol integrates well in the water structure [55, 56] while larger alcohols and polyols introduce more disorder [48, 53]. Even subtle chemical differences, such as between dimethyl sulfoxide (DMSO) and acetone, which differ only by the central sulphur versus carbon atom, can have significant effects on the solution microstructure and structural dynamics [1, 57–60].

The effect of a hydrophobic solute site on water can be viewed as that of an excluded volume, a geometrical constraint or "confinement" which reduces the orientational degrees of freedom for the adjacent water molecules, resulting in limited possibilities to form hydrogen bonds as well as restricted mobility (dynamic slowdown) [34, 61]. At H-donor and H-acceptor solute sites, the difference in hydrogen-bond strengths for water bonded to the solute relative to another water molecule also plays a role, and can ultimately result in either retardation or acceleration of the hydration water dynamics [61, 62]. Thus, in addition to changes in the water structure, solutes can also induce dynamical heterogeneities in water. For example, mapping of the hydration water dynamics around proteins indicates the presence of both "slow" and "fast" water, associated with different surface regions, compared to bulk water [62].

Clearly, the presence of solutes can significantly alter the water structure and dynamics. Inversely, it is hypothesized that HDL/LDL water fluctuations can influence the behaviour of solutes in aqueous solutions, not least in the supercooled regime where the fluctuations proposedly increase. One hypothesized example of water influence is the so-called protein dynamic transition (PDT), below which proteins lose their native biological activity [15, 63, 64]. Specifically, the transition occurs in the supercooled regime at around
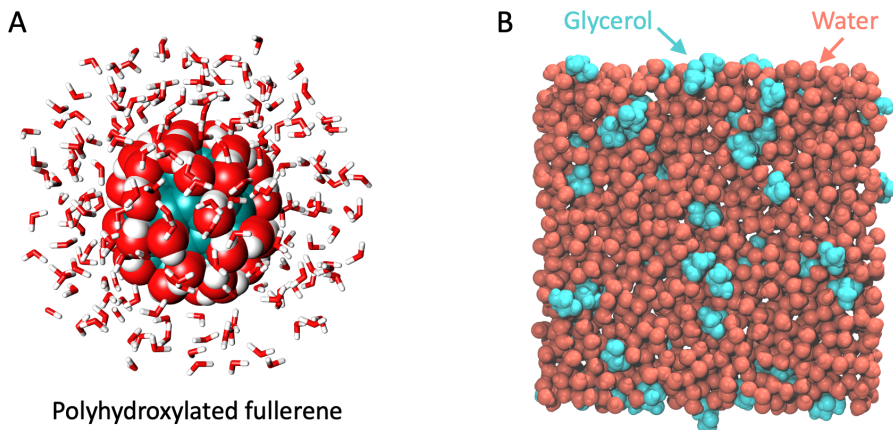
10

A

Polyhydroxylated fullerene

B Glycerol   Water

Figure 2.3: Model systems of solutes in water. (A) A polyhydroxylated fullerene (PHF) molecule surrounded a few layers of water molecules (carbon in cyan, oxygen in red, and hydrogen in white). In *Paper I*, we experimentally study the diffusive dynamics of simple model solutes in the form of spherical nanomolecular probes of varying size, including molecular-sized (≈ 1 nm) PHF. (B) A snapshot from an molecular dynamics (MD) simulation of a mixture of 3.2 mol% glycerol (cyan) and water (red) investigated in *Paper IV*. Adapted from *Paper IV (manuscript)*.

$T \approx 220$ K, indicating that it may be related to the crossover from HDL- to LDL-dominated water at the nearby Widom line [9, 15, 30]. To fully establish the molecular mechanisms of the PDT and other possibly water-induced solute phenomena, investigations of simple model solutes could provide valuable fundamental insights (see examples in Fig. 2.3). For instance, MD simulations of small centrosymmetric hydrophobic solutes, from methane to fullerene, indicate anomalous solute diffusion dynamics in the solute size-dependence of the diffusion coefficient, that violates the Stokes-Einstein relation [14]. Similar to pure water, the SE violation is attributed to caging of the solute and the water jump mechanism, and is remarkably evident already at room temperature though it is more pronounced in the supercooled regime. In *Paper I*, we explore this dynamic anomaly experimentally using nanomolecular probes, including molecular-sized polyhydroxylated fullerenes (PHF) which are water-soluble derivatives of fullerenes (see Fig. 2.3A) [65–70].

2.2.2 The Phase Diagram of Aqueous Solutions

Confinement of water has been a widely used strategy to suppress crystallization in order to measure supercooled water below the homogeneous nucleation temperature, for instance in nanopores [71–73]. The confined space likely

limits ice nucleation and growth, although the mechanisms are not fully understood. Experiments suggest that trapping water in confined spaces can have similar effect as increasing pressure in pure water (see Fig. 2.2) as the disruption of tetrahedral hydrogen bonds, associated with LDL, promotes more disordered HDL-like structures. For instance, X-ray scattering indicates that hydration water confined in the grooves and cavities of proteins overall exhibits a more dense, HDL-like structure compared to that of bulk water [15].

Mixing water with a second component can also create domains of confined water and thereby inhibit freezing of the liquid. For the second component to be an effective *cryoprotectant* it should be a highly water-soluble compound, in order to generate a spatially homogeneous mixture with many small water domains rather than cluster together [57, 58, 60]. Common cryoprotectants used for biological cryopreservation include glycerol (see for example Fig. 2.3B) and DMSO, both of which are small polar-organic molecules that interact strongly with water by hydrogen-bonding [58, 60, 74]. At intermediate molar compositions, these mixtures depress the freezing point of the pure substances by several tens of degrees, and suppress crystallization to the extent that allows supercooling to cryogenic temperatures, even circumventing freezing completely by solidifying into a glassy (amorphous solid) state [60, 75–78]. This kind of obvious influence of solutes on the water structure and dynamics naturally leads to questions, such as to what extent are intrinsic water properties maintained in aqueous solutions. Specifically, do the transitions like the LLT and LLCP indicated in pure supercooled water also manifest in aqueous solutions? If so, in what way are these transitions and the water phase diagram affected by the presence of the solutes?

The mixing water with a solute adds a third dimension to the temperature-pressure phase diagram related to the solute concentration (c), as illustrated in Fig. 2.4. Several studies have indicated the existence of an LLT and LLCP in different aqueous binary mixtures (for $c > 0$), however their proposed locations in the three-dimensional phase diagrams differ. MD simulations and experiments suggest that the addition of solutes (such as NaCl, hydrazinium trifluorophosphate and glycerol) can effectively shift the LLCP location to lower pressures compared to pure bulk water [49, 75, 79, 80]. In these cases, the solutes are often found to promote HDL-like structures reminiscent of bulk water at higher pressures. However, the origin is a bit of a chicken-and-egg situation, either the solutes tend to induce an HDL environment or the solutes preferentially dissolves in HDL domains [49, 79]. The effect is nevertheless similar to moving to higher pressures in the water phase diagram and thereby closer to the LLCP along the pressure axis (see Fig. 2.2). An opposite case is for example found for small hydrophobic Ne atoms, which seemingly favors LDL structures and instead shifts the LLCP to higher pressures [49]. Other
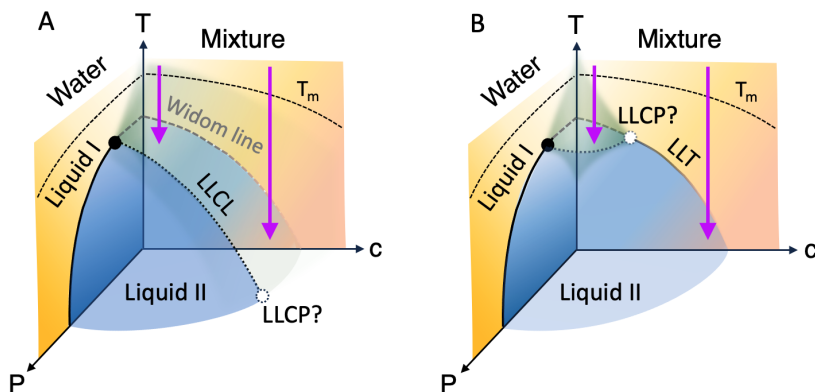
Figure 2.4: Hypothesized phase diagram of binary aqueous solutions which includes three axes – temperature (T), pressure (P) and solute concentration (c). The two panels show examples of two different scenarios proposed in literature for glycerol-water solutions for the location of the liquid-liquid critical point (LLCP) and first-order liquid-liquid transition (LLT, solid line) between two liquid states (liquid I in yellow and liquid II in blue) reminiscent of the high- and low-density liquid (HDL, LDL) in pure bulk water. (A) Scenario A: The mixture LLCP (open dotted circle) is located at elevated pressures and lower temperatures compared to the LLCP bulk water (filled black circle) to which it is connected via a liquid-liquid critical line (LLCL, dotted line). A Widom "surface" extends from the LLCL to ambient pressures where it manifests as a Widom line (grey dashed line). (B) Scenario B: The mixture LLCP is located at ambient pressure in the $T - c$ plane. The purple arrows approximately indicate experiments carried out within this thesis, exploring the hypothesized transitions in the deeply supercooled dilute and intermediate glycerol concentration regimes in the $T - c$ plane at ambient pressure (see *Paper III and IV*).

solutes that have very minor effect on the water structure, as indicated for methanol [55] or LiCl [81], seem to barely shift the LLCP at all at low concentrations. Whether or not the solutes have any preference for solvation in HDL or LDL environments can also drive a possible demixing of the solution [49].

For the glycerol-water system in particular, which is the focus in this thesis (see *Paper III and IV*), the existence and location of the LLCP in the phase diagram has been a topic of debate [75, 76, 82–86]. Experiments on deeply supercooled solutions at intermediate concentrations indicate a possible LLT at ambient pressure, suggesting that the LLCP is located at ambient pressure, as a reflection of the pure water phase diagram in the $T - c$ plane illustrated in Fig. 2.4B (scenario B) [75]. However, other studies in the glassy state of these solutions indicate that glass polymorphism (i.e. HDA and LDA-like glassy states) disappears at higher concentrations (above $c \approx 5$ mol%) and that the observed transitions can be explained by the formation of ice crystallites and

demixing [76, 84, 86]. In line with Fig. 2.4A (scenario A), the LLCP has also been proposed to be located at slightly elevated pressures and at lower temperatures compared to pure bulk water [82]. This hypothesis suggests that the LLCP of pure bulk water and the mixture are connected via a liquid-liquid critical line (LLCL) with a Widom "surface" that extends from the $T - P$ to the $T - c$ plane at ambient pressures. Experimental evidence of a Widom line in deeply supercooled dilute glycerol-solutions ($c < 5$ mol%) has so far been lacking due to the high ice nucleation rate. In *Paper IV*, we therefore utilize rapid evaporative cooling technique [9, 21] to experimentally access this regime, and follow the structural changes in the supercooled liquid by ultrafast X-ray scattering.

3. Probing Liquid Structure and Dynamics with Light- and X-ray Scattering

3.1 Static Light- and X-ray Scattering

In this section, we introduce the fundamental concepts of visible light and X-ray scattering techniques central to this thesis. Unless stated otherwise, the notations and descriptions presented herein are based on Ref. [87, 88].

3.1.1 The Form Factor

Classically speaking, as a wave of light interacts with an electron, the force exerted on the electronic charge by the oscillating electric field causes the electron to oscillate as well, and thus radiate a scattered wave. If the wavelengths of the incident and the scattered wave, λ and λ', are equal the process is known as *elastic scattering*. It follows that the absolute value of the incident wave vector $\mathbf{k}$ equals that of any scattered wave vector $\mathbf{k}'$, i.e. $k' = k = 2\pi/\lambda$. Now, consider the scattering from a second electron at relative position $\mathbf{r}$. The phase difference $\Delta\varphi$ between the incident and scattered waves is given by the difference in the projections of $\mathbf{r}$ onto the incident and scattered beam directions. That is,

$$\Delta\varphi \;=\; (\mathbf{k} - \mathbf{k}') \cdot \mathbf{r} \equiv \mathbf{q} \cdot \mathbf{r}, \tag{3.1}$$

where $\mathbf{q} = \mathbf{k} - \mathbf{k}'$ is the so-called *momentum transfer*, or scattering vector (see schematic in Fig. 3.1). In general, the magnitude of $\mathbf{q}$ for scattering in any medium can be expressed as

$$q \;=\; \frac{4\pi n_0}{\lambda} \sin\left(\frac{\theta}{2}\right), \tag{3.2}$$

where θ is the angle between the incident and scattered wave vectors and n_0 is the refractive index of the medium. However, in the case of X-rays, the refractive index, which is frequency-dependent, nearly equals unity and is for this reason usually neglected.
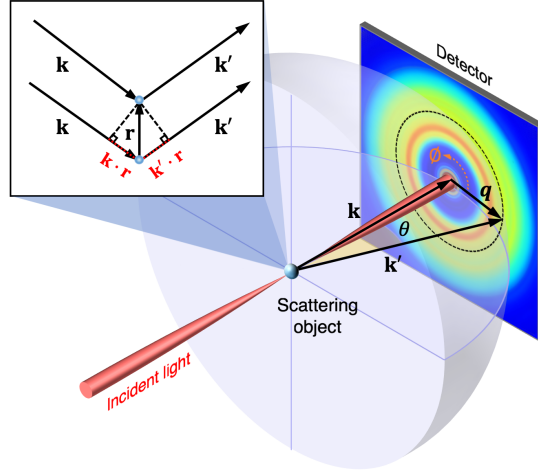
Figure 3.1: The geometry of a general scattering experiment. An incident light beam hits a scattering object and the intensity of the scattered light is measured by a detector. The scattered intensity depends on the scattering angle θ which relates to the momentum transfer q by eq. (3.2). Here, the black arrows indicate the wavevectors of the incident and scattered beams, $\mathbf{k}$ and $\mathbf{k}'$, as well as the scattering vector or momentum transfer $\mathbf{q} = \mathbf{k} - \mathbf{k}'$. The zoomed-in inset illustrates how the scattering process and $\mathbf{q}$, according to eq. (3.1), relate to length scales $\mathbf{r}$ in real space. That is, large q (large scattering angles θ) relates to small length scales r in real space and vice versa. The dotted orange arrow indicates the azimuthal angle ϕ.

The phase difference between the incident and scattered waves leads to constructive and destructive interference, with a resulting scattering amplitude that varies with q, or likewise, the scattering angle θ. In particular, the scattering amplitude that results from the scattering from all the electrons of an atom is known as the *atomic form factor* f^0 and may be written as

$$f^0(\mathbf{q}) = \int \rho(\mathbf{r}) \, e^{i\mathbf{q}\cdot\mathbf{r}} d\mathbf{r}, \tag{3.3}$$

in units of $-r_0$, where r_0 is the Thomson scattering length, or the classical radius of the electron, $\rho(\mathbf{r})$ is the number density of electrons and $e^{i\mathbf{q}\cdot\mathbf{r}}$ is known as the phase factor. As can be noticed, the form factor $f^0(\mathbf{q})$ is merely the *Fourier transform (FT)* of the electron density in real space $\rho(\mathbf{r})$ into momentum transfer q-space, or *reciprocal space*. The latter emphasizes the inverse relation between q and real space length r, where $r \sim 2\pi/q$ such that large q relates to small length scales in real space and vice versa.

Moreover, the total scattering from the atoms in a molecule is given by the sum of the single-atom contributions, with their corresponding phase factors

to account for the inter-atomic interference. This is known as the *molecular form factor*,

$$f(\mathbf{q}) = \sum_j f_j^0(\mathbf{q})\, e^{i\mathbf{q}\cdot\mathbf{r}_j}, \tag{3.4}$$

where f_j^0 is the atomic form factor for atom j. The resulting scattered intensity $I(q)$ is proportional to the absolute square of the scattering amplitude, and may be expressed as $I(q) = |f(q)|^2$ (in dimensionless units).

Over larger length scales, equivalent to small q (small scattering angles θ), as in a material, the amplitude of the phase factor is expressed in terms of the scattering length density ρ_{sl}. For a single-component material $\rho_{sl} = f\bar{\rho}$ (in units of r_0), where $\bar{\rho}$ is the average number density. The long-range order (LRO), or small-angle scattering intensity, is then

$$I_{LRO}(q) = \left| \int_V \rho_{sl}\, e^{i\mathbf{q}\cdot\mathbf{r}}\, dV \right|^2. \tag{3.5}$$

Thus, the form factor of any shaped material can be derived by integrating the scattering elements over the volume V of the shape. In particular, for a single-component spherical particle with radius R and volume V_p, such as a nanoparticle, one finds that the *single-particle form factor* $F_p(q)$ becomes

$$F_p(q) = \frac{1}{V_p\rho_{sl}} \left| \int_{V_p} \rho_{sl} e^{i\mathbf{q}\cdot\mathbf{r}}\, dV_p \right| = 3\left[\frac{\sin(qR) - qR\cos(qR)}{(qR)^3}\right]. \tag{3.6}$$

Here, by definition, the particle form factor is normalized by the integrated volume V_p and ρ_{sl}. The scattering intensity from dilute nanoparticle solutions, i.e. absence of inter-particle correlations, is thus given by $I_p(q) = \Delta\rho_{sl}^2 V_p^2 |F_p(q)|^2$.

3.1.2 The Structure Factor of a Liquid

Similarly to deriving the scattering intensity for a molecule, the scattering intensity from a system of N molecules, such as a liquid or a glass, can be derived from its components as

$$I(\mathbf{q}) = \left| \sum_n^N f_n(\mathbf{q})e^{i\mathbf{q}\cdot\mathbf{r}_n} \right|^2 = \sum_n^N \sum_m^N f_n(\mathbf{q})f_m(\mathbf{q})e^{i\mathbf{q}\cdot(\mathbf{r}_n-\mathbf{r}_m)}. \tag{3.7}$$

where $f_n(\mathbf{q})$ is the form factor of molecule n at position $\mathbf{r}_n$. By separating the terms for which $n = m$ (self-scattering, I_{self}) and $n \neq m$ (cross-term, I_{cross}), we get

$$I(\mathbf{q}) = \sum_n^N f_n^2(\mathbf{q}) + \sum_n^N \sum_{m\neq n}^N f_n(\mathbf{q})f_m(\mathbf{q})e^{i\mathbf{q}\cdot(\mathbf{r}_n-\mathbf{r}_m)} = NI_{self}(\mathbf{q}) + I_{cross}(\mathbf{q}) \tag{3.8}$$

17

The self-scattering term represents the scattering from N independent molecules, as would be the case in a gas-phase system where the molecules are far apart. By contrast, the cross-term results from the interference between the molecules and therefore contains information about their spatial arrangement, i.e. the intermolecular structure of the system. The self-scattering term can be reformulated as a sum for each molecular species j,

$$NI_{self}(\mathbf{q}) = \sum_n^N f_n^2(\mathbf{q}) = N\sum_j^J x_j f_j^2(\mathbf{q}), \qquad (3.9)$$

where J is the total number of molecular species, N_j is the number of molecules of species j and $x_j = N_j/N$ is the molar fraction. For instance, in *Paper IV*, we study a mixture of glycerol (g) and water (w), and so $I_{self} = x_g f_g^2 + x_w f_w^2$.

By introducing the average density $\bar{\rho}$, and the local number density $\rho_n(\mathbf{r}_{nm})$ in volume-element dV_m positioned at $\mathbf{r}_m$ with respect to reference position $\mathbf{r}_n$, we can rewrite eq. (3.8) as

$$I(\mathbf{q}) = NI_{self}(\mathbf{q}) + \sum_n^N \int_V f_n(\mathbf{q})f_m(\mathbf{q})[\rho_n(\mathbf{r}_{nm}) - \bar{\rho}]e^{i\mathbf{q}\cdot(\mathbf{r_n}-\mathbf{r_m})}dV_m +$$

$$+ \sum_n^N \int_V f_n(\mathbf{q})f_m(\mathbf{q})\bar{\rho}e^{i\mathbf{q}\cdot(\mathbf{r_n}-\mathbf{r_m})}dV_m. \quad (3.10)$$

The term on the second row can further be reformulated to

$$\sum_n^N f_n(\mathbf{q})e^{i\mathbf{q}\cdot\mathbf{r_n}} \int_V \bar{\rho}f_m(\mathbf{q})e^{-i\mathbf{q}\cdot\mathbf{r_m}}dV_m =$$

$$\int_V \bar{\rho}f_n(\mathbf{q})e^{i\mathbf{q}\cdot\mathbf{r_n}}dV_n \int_V \bar{\rho}f_m(\mathbf{q})e^{-i\mathbf{q}\cdot\mathbf{r_m}}dV_m = \left| \int_V \bar{\rho}\langle f(\mathbf{q})\rangle e^{i\mathbf{q}\cdot\mathbf{r}}dV \right|^2. \quad (3.11)$$

We can notice that this term resembles the expression given in eq. (3.5), but for a multi-component system, and describes the scattering for long-range order. Destructive interference results in that this term only contributes significantly in the small-angle scattering regime, i.e. as $q \to 0$. In contrast, the term in the upper row of eq. (3.10) contributes most where the deviation from the average density is large, which is the case at small distances r (large q) relating to the local inter-molecular structure, or short-range order (SRO). The deviation from the average density rapidly falls off and becomes negligible at large distances (small q).

For an isotropic system, which usually holds for disordered systems like liquids and glasses, we can simplify the eq. (3.10) by averaging of different reference points such that $\langle\rho_n(\mathbf{r}_{nm})\rangle \to \rho(\mathbf{r})$ and use the average scattering

amplitude for each pair of molecules (n and m) in the cross-term, $\langle f(\mathbf{q}) \rangle^2 = (\sum_j^J x_j f_j)^2$. Hence, we can rewrite eq. (3.10) as

$$I(\mathbf{q}) = NI_{self}(\mathbf{q}) + N\langle f(\mathbf{q}) \rangle^2 \int_V [\rho(\mathbf{r}) - \bar{\rho}]e^{i\mathbf{q}\cdot\mathbf{r}}dV +$$

$$+\bar{\rho}N\langle f(\mathbf{q}) \rangle^2 \int_V e^{i\mathbf{q}\cdot\mathbf{r}}dV \ . \qquad (3.12)$$

Averaging along the azimuthal angle (see Fig. 3.1) further allows to drop the vector notation. Integration over spherical shells $dV = 4\pi r^2 dr$ and rewriting in terms of the *radial distribution function* $g(r) = \rho(r)/\bar{\rho}$, which describes the variation in the local number density from the average (i.e. unity), then yields

$$I(q) = NI_{self}(q) + N\langle f(q) \rangle^2 \int_0^\infty \bar{\rho}[g(r) - 1]\frac{\sin(qr)}{qr}4\pi r^2 \ dr +$$

$$+N\langle f(q) \rangle^2 \int_0^\infty \bar{\rho}\frac{\sin(qr)}{qr}4\pi r^2 \ dr \ . \qquad (3.13)$$

To highlight the intermolecular structure (the cross-term I_{cross} in eq. (3.8)), the scattering intensity of a liquid or glassy system is commonly expressed as the scattering intensity normalized by the number of molecules N and the self-scattering term I_{self}:

$$S(q) = \frac{I(q)}{NI_{self}(q)} = 1 + \frac{I_{cross}(q)}{NI_{self}(q)} \qquad (3.14)$$

$S(q)$ is known as the *structure factor* and oscillates asymptotically around unity such that $\lim_{q \to \infty} S(q) = 1$ (see Fig. 3.2). This trend reflects the decreasing deviation from the scattering of isolated molecules as one approaches larger q, i.e. small length scales for which influence from inter-molecular correlations decreases. It is conventional to express the structure factor using only the short-range order term. In a dilute solution, $\langle f(q) \rangle^2 \simeq I_{self}$, and the structure factor therefore simplifies to

$$S_{SRO}(q) \simeq 1 + \int_0^\infty 4\pi r\bar{\rho}[g(r) - 1]\frac{\sin(qr)}{q} \ dr, \qquad (3.15)$$

In other words, the structure factor $S(q)$ and the radial distribution function $g(r)$ are related by Fourier Transform, and so the structure factor may be described as the reciprocal q-space analogue of the real-space local structure.

It may be pointed out here that the length scales, and equivalent q-ranges, for short- and long-range order are indeed relative and system-specific. In general, though, the scattering at large q ($q \gtrsim 1$ Å^{-1}), related to short-range order at inter-atomic distances, is referred to as *wide-angle X-ray scattering*
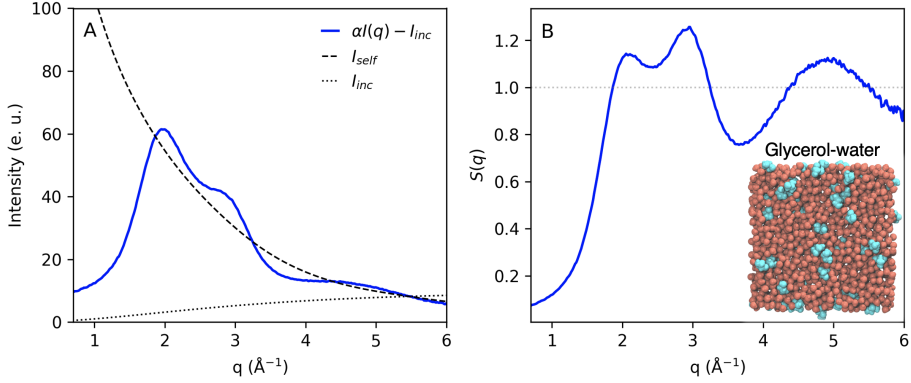
Figure 3.2: The scattering intensity and structure factor of a liquid. (A) The scattering intensity $I(q)$ from 3.2 mol% glycerol-water solution (from *Paper IV*) normalized to the intensity per molecule in electron units (e.u.) by the normalization factor α, related to the number of molecules (N) and determined with the Krogh-Moe method [89, 90] (see *Paper IV*). By subtracting the incoherent scattering I_{inc} (dotted line), the blue solid line shows only the coherent scattering intensity which decays around the molecular form factor I_{self} (i.e. the self-scattering, dashed line). (B) The resulting structure factor $S(q)$ of the glycerol-water solution according eq. (3.14) oscillates around unity. The inset shows a snapshot of a molecular dynamics (MD) simulation of the solution. Adapted from *Paper IV (manuscript)*.

(WAXS), while the scattering at small q, sensitive to nanometer scale structures, is known as *small-angle X-ray scattering (SAXS)*. The latter extends to even smaller q and micrometer scales with visible light scattering. Nevertheless, for a system with a hierarchical structure, such as a colloidal suspension, short-range order may likewise refer to the single-particle shape (i.e. the single-particle form factor $F_p(q)$) with the local inter-particle arrangements described by the structure factor $S_p(q)$. Thus, in the small-angle scattering regime, the scattering intensity from a suspension of particles is given by

$$I_p(q) = \Delta\rho_{sl}^2 V_p^2 |F_p(q)|^2 S_p(q). \qquad (3.16)$$

Since $S_p(q) \to 1$ in the dilute limit, eq. (3.16) for a dilute particle solution is simplified to $I_p(q) = \Delta\rho_{sl}^2 V_p^2 |F_p(q)|^2$.

3.1.3 The Liquid Structure Factor in the Presence of Density fluctuations

We know from eq. (3.12)-(3.15) that the structure factor $S(q)$ is sensitive to local density fluctuations, $[\rho(r) - \bar{\rho}]$. Such density fluctuations become particularly significant close to critical points of phase transitions, at which the

fluctuations become so large that they extend to macroscopic length scales and, thus, accompanied by a dramatic increase of scattering intensity at $q \to 0$. For water, specifically, this is the case around the Widom line, along which the fluctuations of HDL and LDL locally maximize, and of course most substantially at the hypothesized LLCP, the global maximum [8, 9]. The Widom line has been indicated in experiments on pure water [9], while the LLCP has not yet been directly verified experimentally [10]. In *Paper IV*, we experimentally measure the enhancement of density fluctuations in evaporatively supercooled droplets of dilute glycerol-water solution by ultrafast SAXS, indicative of the existence of HDL-LDL-like liquid fluctuations also in aqueous solutions.

The scattering from a normal liquid (S_N), in absence of critical fluctuations, can be described with the Percus-Yevick (PY) structure factor for a hard-sphere fluid [91, 92]

$$S_N(q) = 1 - 12\psi \left[\frac{\psi(3 - \psi^2) - 2}{(1 - \psi)^4} \right] \left(\frac{j_1(2Rq)}{2Rq} \right) \qquad (3.17)$$

where R is the hard-sphere radius and $\psi = \frac{4}{3}\pi R^3 \bar{\rho}$ is the volume fraction occupied by the particles. This function generates a structure factor peak arising from the local inter-particle correlations which decreases asymptotically to a constant value as $q \to 0$ (see Fig. 3.3D). In the presence of critical fluctuations in the liquid, spatial variations in the density gives rise to an excess, anomalous scattering contribution (S_A) that results in enhanced SAXS intensity, wherefore the total structure factor in the SAXS region can be described as the sum of the normal and anomalous component [9, 93]:

$$S_{tot} = S_N + S_A, \qquad (3.18)$$

Moreover, the anomalous scattering may, according to Orstein-Zernike theory, be expressed as [94–96]

$$S_A(q) = \frac{S_A(0)}{1 + \xi^2 q^2} \qquad (3.19)$$

Here, $S_A(0)$ is the excess anomalous scattering at $q = 0$ and ξ is the correlation length. The latter can be related to the width of the the exponentially decaying amplitude of the radial distribution function $g(r)$ with increasing distance r, or more intuitively to the size of the fluctuation domains.

The magnitude of the density fluctuations also influences the total intercept $S_{tot}(0)$ since

$$S_{tot}(0) \simeq \bar{\rho} k_B T \kappa_T, \qquad (3.20)$$

where the isothermal compressibility κ_T is directly related to fluctuations (i.e. variance) in the number of particles N within a constant volume V by

$$\langle (N - \bar{N})^2 \rangle_{VPT} = \bar{N} \bar{\rho} k_B T \kappa_T, \qquad (3.21)$$
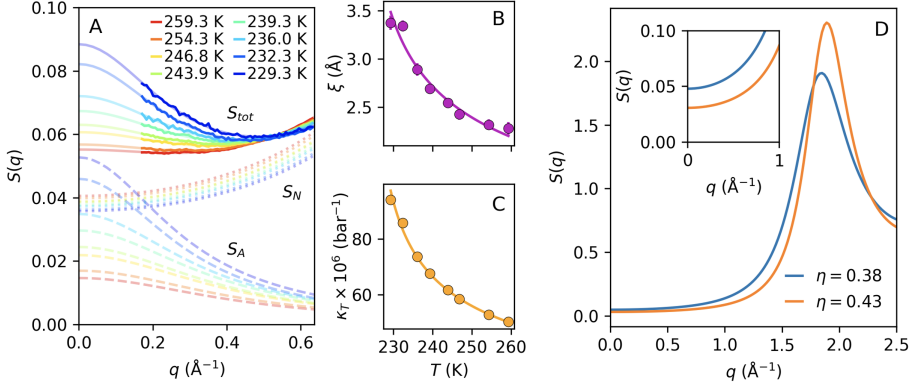
Figure 3.3: Small-angle X-ray scattering (SAXS) of a liquid. (A) ULtrafast SAXS of evaporatively supercooled microdroplets of 3.2 mol% glycerol-water solution at different temperatures (bright solid lines). Solid shaded lines indicate fits of the experimental data to eq. (3.18) which is decomposed into normal (dotted lines, eq. (3.17)) and anomalous (dashed lines, eq. (3.19)) components. The fitted correlation length ξ and isothermal compressibility are shown in panel (B) and (C), where the solid lines indicate power law fits according to eq. (3.23). (D) Examples of the Percus-Yevick approximation of the scattering of a hard-sphere fluid (the normal component) given in eq. (3.17) for radius $R = 1.8$ Å with different volume fractions η. Larger η results in an enhancement and a shift of the structure factor peak towards larger q, while the plateau intensity at $q \to 0$ is decreased. (A-C) Reprinted from *Paper IV (manuscript)*.

or in terms of volume fluctuations for a constant number of particles,

$$\langle (V - \langle V \rangle^2 \rangle_{NPT} = \bar{V} k_B T \kappa_T. \tag{3.22}$$

Upon approaching a critical point, the critical fluctuations grow larger and become more pronounced, resulting in that the compressibility and correlation length strongly increase with power-law behaviour [94, 97]:

$$\xi(T) = \xi_0 \varepsilon^{-\nu}, \quad \kappa_T(T) = \kappa_{T,0} \varepsilon^{-\gamma} \tag{3.23}$$

with $\varepsilon = (T - T_s)/T_s$, where T_s is the singular temperature at which the property diverges, and ν and γ are the power law exponents which theoretically maximize at values $\nu = 0.6$ and $\gamma = 1.2$, or $\nu/\gamma = 0.5$ at the critical point [96, 98]. ξ_0 and $\kappa_{T,0}$ are constants.

In principle, eq. (3.20) applies only to an ideal solution in which the components are always uniformly distributed. Otherwise, for a two-component system, the structure factor at $q = 0$ has an extra term arising from concentra-

tion fluctuations $\langle (x - \bar{x})^2 \rangle$ [99]:

$$\begin{aligned} S_{tot}(0) &= \bar{\rho} k_B T \kappa_T + \frac{(\bar{Z} \Delta v \bar{\rho} - \Delta Z)^2}{\bar{Z}^2} S_{CC}(0), \\ S_{CC}(0) &= \bar{N} \langle (x - \bar{x})^2 \rangle, \end{aligned} \tag{3.24}$$

where $\bar{Z} = x_1 Z_1 + x_2 Z_2$ is the weighted average number of electrons per compo-nent, ΔZ is the difference in the number of electrons while δv is the difference in partial molar volumes between the two components. x is again the molar fraction.

3.2 Structural Dynamics from Speckle Intensity Fluctuations

3.2.1 Speckle Intensity Fluctuations

Consider a coherent light source directed at a sample containing a liquid suspension of particles. Light scatters from the particles in the solution but, since the instantaneous positions of the particles are random and disordered, the scattered intensity captured by a detector in an instant snapshot exhibits what is known as *speckles* – seemingly randomly distributed bright spots arising from the interference of light scattered from a disordered system (see Fig. 3.4). As the particles move around in the liquid, thus changing their positions, the speckle pattern measured at subsequent time points varies too and give rise to intensity fluctuations, as illustrated in Fig. 3.5. In other words, the temporal *speckle intensity fluctuations* reflect the *structural dynamics* within the sample, although in reciprocal space [100].

The shorter the acquisition time for a speckle pattern, the higher the speckle contrast, whilst integration of the scattered intensity over a time longer than the characteristic dynamic time scale smears out the speckles and eventually results in an average intensity, reflecting only the average sample structure. For instance, the average intensity for a dilute solution of particles would be proportional to the absolute square of the single-particle form factor, as in eq. (3.16). Specifically, the speckle contrast, or visibility V_2, is defined as [101]

Figure 3.4: Speckles represent the instantaneous structure of a disordered system in reciprocal space. Thus, a real image is related to its speckle pattern by Fourier transform (FT).

$$V_2 = \frac{\langle I(q)^2 \rangle - \langle I(q) \rangle^2}{\langle I(q) \rangle^2} \qquad (3.25)$$

and thus relates to the variance of the intensity, or the relative difference in intensity between bright and dark spots in a speckle pattern. A prerequisite for resolving speckles, i.e. obtaining sufficient speckle contrast, is that the light source is highly *coherent* [102]. The higher the degree of coherence, the more complete constructive and destructive interference of the scattered light waves, and thus increased speckle contrast. In addition, the incident *coherent flux* needs to be high enough to generate sufficient scattered intensity on the detector, in order for a measurable signal to be attained within the acquisition time required to resolve the dynamics of interest. There are two kinds of coherence – *longitudinal* and *transverse coherence*. The former, longitudinal (or temporal) coherence, is related to the
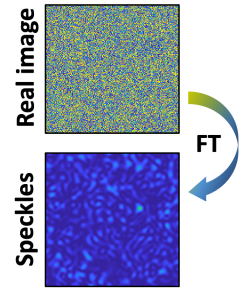
spectral bandwidth $\Delta\lambda$. A narrow bandwidth, as in monochromatic light, results in a long longitudinal coherence length $\varepsilon_l = \lambda^2/2\Delta\lambda$ [87]. Transverse (or spatial) coherence, on the other hand, refers to the spatial uniformity of the light wavefront. The small angular divergence of a highly directed light beam is said to have high transverse coherence or long transverse coherence length $\varepsilon_T = \lambda R/2D$, where R is the distance from the source with size D [87].

Lasers are highly coherent light sources and, thus, ideally suited for generating speckle patterns and for extracting dynamic information from the analysis of speckle intensity fluctuations. The use of visible lasers for measuring speckle dynamics is widely known as *dynamic light scattering (DLS)* [100].

3.2.2 Dynamic Light Scattering

Fig. 3.5 shows a schematic of the DLS setup (LS instruments) used in this thesis work (*Paper I*). Here, the incident light is a continuous-wave (CW) laser with wavelength $\lambda = 660$ nm and a maximum output power of 500 mW. The laser is focused onto the sample consisting of a sample solution, e.g. a dilute nanoparticle dispersion, contained in a quartz glass capillary. In addition, the sample is immersed in a bath of decalin (index-matching liquid) connected to an external thermostat, by which the sample temperature is controlled.

Scattered light is measured at a scattering angle θ, corresponding to momentum transfer $q = \frac{4\pi n_0}{\lambda} \sin\left(\frac{\theta}{2}\right)$, using a duplicate set of photon detectors mounted on a rotatable goniometer arm. The reason for the use of two photon detectors is to enable correlation of the two simultaneously recorded scattering signals, so-called pseudo-correlation, which reduces the effect of detector after-pulsing (when the hit of a single photon generates more than one electrical pulse, i.e. more than one photon count [103]) and increases the time resolution, in this case up to 12.5 ns. Moreover, the photon detectors are connected to a correlator which automatically temporally correlates the measured speckle intensity fluctuations, yielding the so-called *intensity autocorrelation g_2 function*.

Conventional DLS suffers from the drawback of inaccurate dynamic measurements of concentrated sample solutions. The measured anomalies arise from multiple scattering events, i.e. when the incident light scatters more than once before exiting the sample. However, the DLS setup presented here offers the use of a special experimental mode, called 3D mode, that enable suppression of multiple scattering from concentrated samples to some extent. This mode utilizes a beam splitter in front of the sample that separates the incident laser beam in two, both of which are focused onto the same spot within the sample. In principle, this enables a simultaneous measurement of two scattering experiments. Unless multiple scattering occurs, the two scattering experi-
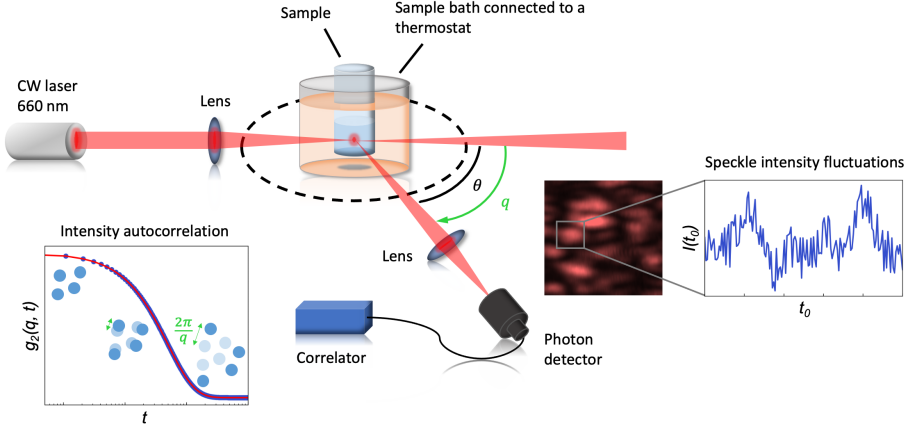
Figure 3.5: Dynamic light scattering (DLS). A schematic overview showing the general principle of DLS and the experimental setup (from LS instruments) used in Paper I. A continuous-wave laser is focused onto the sample and scattered light is measured at different scattering angles θ (or momentum transfers q) by the photon detector mounted on a rotatable goniometer arm. The recorded speckle intensity fluctuations (shown schematically on the right) are temporally correlated using a built-in correlator to yield the intensity autocorrelation g_2 function (see lower left). Moreover, the decay of the g_2 function relates to the sample dynamics, with the length scale of the dynamics linked to q roughly by $2\pi/q$.

ments measured by the two photon detectors should perfectly correlate, or else their cross-correlation diminishes the signal.

3.2.3 The Intensity Autocorrelation Function

Useful dynamic information from speckle intensity fluctuations can be extracted by temporal correlation of the intensity. Particularly, the temporal intensity autocorrelation g_2 function is computed as [100, 104]

$$g_2(q,t) = \frac{\langle I(q,t_0)I(q,t_0+t)\rangle}{\langle I(q,t_0)\rangle^2}, \tag{3.26}$$

where $I(q,t_0)$ and $I(q,t_0+t)$ is the intensity at time t_0 and after lag time t, respectively. As is commonly the case, the dimension of the scattering volume, i.e. the focus size, is large compared to the probed characteristic length scale in real space $r \sim 2\pi/Q$ and the scattering volume contains a large number of scatterers. For example, visible lasers used for DLS give access to $q \sim 0.01$ nm^{-1}, or $2\pi/q \sim 600$ nm, while the focus size is typically in the order of 100 μm. In this scenario, number fluctuations arising from scatterers entering and leaving the volume can be neglected and the intensity fluctuations are governed by

structural fluctuations, due to dynamic displacements of scatterers within the focus. Such dynamic correlations are described by the dynamic structure factor $f(q,t)$ [37, 102], also known as the *intermediate scattering function*. For scattering from one type of atom (e.g. from oxygens in water), [102, 105],

$$f(q,t) = \frac{1}{N} \left\langle \sum_{i=1}^{N} \sum_{j=1}^{N} e^{i\mathbf{q}\cdot[\mathbf{r}_i(t)-\mathbf{r}_j(t)]} \right\rangle, \tag{3.27}$$

where N is the average number of scattering atoms. Eq. (3.26) is then given by the *Siegert relation* [100, 102, 104, 105]:

$$g_2(q,t) = 1 + \beta(q)|f(q,t)|^2. \tag{3.28}$$

Here, $0 < \beta \leq 1$ refers to the speckle contrast and depends on experimental parameters, in particular the coherence of the incident light as already mentioned, but additionally on parameters such as the focus and detector pixel size [106]. In the ideal experiment, $\beta = 1$ and g_2 decreases from an initial value of 2 to 1, as $f(q,t)$ decays from 1 to 0, with a time constant τ related to the dynamic time scale [100, 102, 104]. In general,

$$f(q,t) = e^{-(t/\tau_0(q))^{\alpha(q)}}, \tag{3.29}$$

where $0 < \alpha \leq 2$ is the Kohlrausch-Williams-Watts (KWW) constant [107]. The average relaxation time constant is given by $\tau = \frac{\tau_0}{\alpha}\Gamma(\frac{1}{\alpha})$, where Γ is the Gamma distribution function.

A illustrative summary of different types of motions is presented in Fig. 3.6A. For simple diffusive dynamics, the KWW exponent in eq. (3.29) equals unity, $\alpha = 1$, while $\alpha < 1$ is usually attributed to heterogeneity that results from a broad distribution of relaxation times [108]. The latter can either be associated with dynamical heterogeneities (heterogeneities in the time domain), such as cage effects, or be due to spatially heterogeneous dynamics, such as in a sample where distinct spatial domains give rise to slightly different dynamics [109]. A multi-component system, such as one containing diffusing nanoparticles with a broad distribution of particle sizes, can also result in a distribution of relaxation times which yields $\alpha < 1$ (see *Paper I*) [13]. In contrast, a compressed KWW exponent $\alpha > 1$ has been associated with non-diffusive dynamics in jammed systems or super-diffusive dynamics during LLTs [110–114].

Different types of motion also exhibit characteristic q-dependence for the relaxation time τ. For directional, so-called ballistic motion, τ^{-1} is linearly dependent on q. In contrast, sub-diffusive motion, often involving cage effects, is associated with a fractional dependence where $\tau^{-1} \propto q^{1/n}$ and $n > 1$ [37, 111,
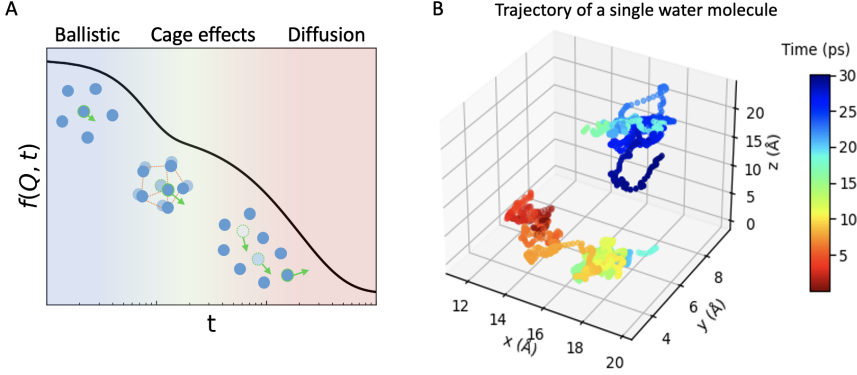
Figure 3.6: (A) Different types of motions exhibited in a liquid system; At the shortest time scales the particles undergoes ballistic (directional) motion. As the particle attempts to escape the cage of surrounding liquid, the motion is slowed down and re-directed, giving rise to caged dynamics (cage effects). The effective motion resulting from small random steps over long time and length scales, is known as diffusion. (B) A trajectory of a single water molecule from a molecular dynamics simulation of liquid water, highlighting the strong cage effects from the hydrogen bonding that leads to a jump-like diffusive motion.

115]. For purely diffusive motion, on the other hand, τ^{-1} displays a typical quadratic dependence on q with a slope equal to the diffusion coefficient D, i.e. $\tau^{-1} = Dq^2$ [12, 13]. In such case, exponent in eq. (3.29) can be directly related to the mean-squared displacement (MSD), $\langle r^2 \rangle = 6Dt$, such that $t/\tau = \frac{1}{6}\langle r^2 \rangle q^2$. The diffusion coefficient can be also related to the hydrodynamic radius R_h of the diffusing species and the viscosity of the medium η by the *Stokes-Einstein (SE) relation* [116]. In particular, for a spherical particle the SE relation is given by

$$D = \frac{k_B T}{6\pi R_h \eta(T)},\tag{3.30}$$

where k_B is the Boltzmann constant and T is the temperature.

3.2.4   X-ray Photon Correlation Spectroscopy

Based on similar principles as DLS, dynamic information from speckle intensity fluctuations can be obtained using parts of the electromagnetic spectrum other than visible light. In fact, different photon energies (wavelengths) enable access to different ranges in momentum transfer q-space and, thus, to different length scales $r \sim 2\pi/q$ in real space. In particular, probing structural dynamics on molecular to atomic length scales, i.e. from tens of nanometers to Ångstroms (atomic distances), requires photon energies in the order of
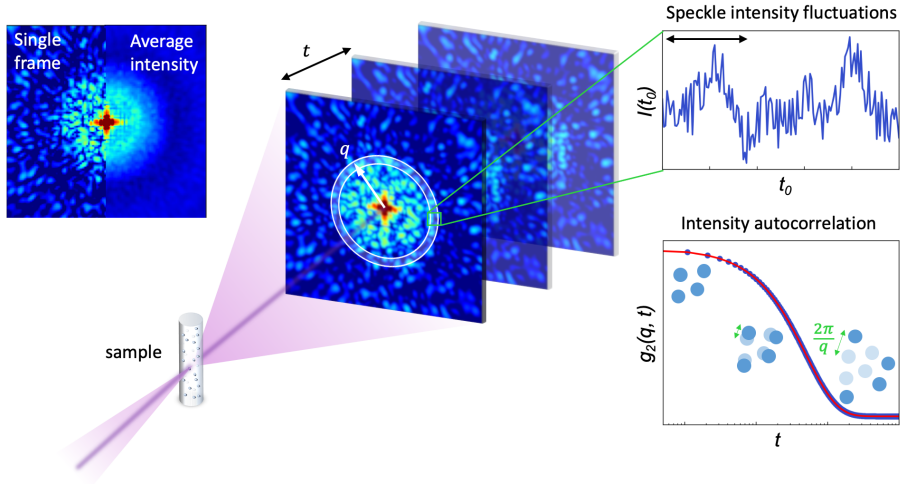
Figure 3.7: A schematic of a standard X-ray photon correlation spectroscopy (XPCS) experiment. The X-ray scattering from the sample is recorded as a time series of speckle patterns using a 2D detector. Next, the speckle intensity fluctuations in detector pixels within concentric rings around the beam center, corresponding to different q-values, are time-correlated to yield correlation functions such as g_2 (right). The time resolution is given by the time separation Δt between the recorded detector images, which is limited by the detector frame rate.

keV, or wavelengths of about 1 Å, corresponding to that of X-ray radiation. This structural sensitivity of X-rays is utilized in the X-ray analogue of DLS, known as *X-ray photon correlation spectroscopy (XPCS)* [3, 102, 117–121]. In addition, XPCS has the advantage of largely increased attenuation length of X-rays compared to visible light used in DLS. This also allows XPCS to measure dynamics in highly concentrated, opaque solutions or solid samples [3, 106, 122].

A schematic of a standard XPCS experiment is shown in Fig. 3.7. Again, the principle is the same as for DLS. An incident beam of coherent X-ray radiation (see more details in section 3.3) is focused onto the sample, which scatters the X-rays and generates a speckle pattern representing the instantaneous structure of the sample. During the experiment a time series of speckle patterns are recorded using a large 2D detector placed at a distance L behind the sample. The use of a 2D detector allows a broad momentum transfer q-range to be measured simultaneously, where different q:s are represented by concentric rings around the direct beam, as depicted in Fig. 3.7. To extract the dynamical information, the speckle intensity in the consecutively recorded frames is time-correlated, pixel by pixel, to yield correlation functions such as g_2 given in eq. (3.26). The many pixels in each q-ring enable statistical aver-

aging of the temporal correlation over pixels p, in addition to averaging over initial times t_0, as represented by the brackets in eq. (3.26).

Resolving Heterogeneous Dynamics with Higher Order Correlations

A major advantage of XPCS is the possibility to resolve heterogeneous dynamics by analysis of higher order intensity correlation functions. Such dynamical processes include, among others, beam-induced dynamics [123], phase transitions [12], glass formation and aging processes [124], as well as spatial sample fluctuations [125]. The latter include for instance spin fluctuations in magnetic systems [126], and potentially in liquids, as is the interest of this thesis. Specifically, the two-time intensity correlation (TTC) function c_2 [127] provides the temporal evolution of the sample dynamics, i.e. the variation of the one-time intensity correlation function g_2 during the measurement time. It is computed as

$$c_2(q,t_1,t_2) = \frac{\langle I(q,t_1)I(q,t_2)\rangle_{\text{pix}}}{\langle I(q,t_1)\rangle_{\text{pix}}\langle I(q,t_2)\rangle_{\text{pix}}}, \tag{3.31}$$

where $I(q,t_1)$ and $I(q,t_2)$ is the speckle intensity at the time points t_1 and t_2 (i.e. different frames in XPCS), respectively. With a 2D detector, as in XPCS, the intensity correlation is averaged over all pixels within the specified q-ring, having finite width dq (see Fig. 3.7). In contrast to the one-time correlation function g_2, there is no temporal averaging for c_2, only pixel-averaging, as emphasized by the subscript 'pix'.

Speckle Contrast in XPCS Experiments

One of the most important aspects to consider in an XPCS experiment is the speckle contrast β. The higher the speckle contrast, the higher the signal-to-noise ratio of intensity correlation functions, such as the g_2 function in eq. (3.28) [102]. Firstly, the acquisition time of each measured scattering image needs to be shorter than the time scale of the probed dynamics, otherwise the motions within the sample smear out the speckles (see section 3.2.1). Additionally, the speckle contrast depends on several experimental settings, independent of the sample dynamics, including the X-ray beam focus size σ (see *Paper II*) [128] and wavelength λ, sample-to-detector distance L, detector pixel size P, sample thickness d, momentum transfer q, and last but not least the coherent properties of the X-rays [106].

Full resolution of a speckle pattern is attained only when the average size of the measured speckles are at least as large as the detector pixel size, which is typically about $50-200~\mu$m. Moreover, the speckle size is related to the

beam size and sample-to-detector distance L by [106]

$$S = L\lambda/\sigma, \qquad (3.32)$$

where λ is the X-ray wavelength. Optimizing the relation between beam size and sample-to-detector distance to, as much as possible, fulfill the above-mentioned criteria is therefore a key step in the XPCS experimental design. Since beam sizes are generally limited to a few μm, XPCS experiments often require very long experimental stations at the X-ray radiation facilities, in the order of $5 - 20$ m. On the other hand, there is often a trade-off between long sample-to-detector distance with high contrast versus high scattering intensity on the detector, since the latter decreases with larger distance.

3.2.5 Nanofocused X-ray Photon Correlation Spectroscopy

A small X-ray beam focus size σ does not only increase the speckle contrast, but also the spatial resolution of the sample, and thus the possibility to probe the sample dynamics locally [129]. The outstanding coherent properties of the new generation synchrotron X-ray radiation sources (see details in section 3.3), such as MAX IV Laboratory in Lund, Sweden, enable nanofocused beam sizes in the order of ≈ 100 nm [130, 131]. Especially for heterogeneous samples, a nanofocus can potentially enhance the sensitivity to spatial heterogeneities, including nanoscale liquid fluctuations (see Fig. 3.8A). This is the main idea behind combining X-ray nanofocusing and XPCS, so-called *nanofocused XPCS (nano-XPCS)*. In addition, the multifold contrast increase seen for nanofocused beam sizes (see *Paper II*) allows to carry out synchrotron XPCS experiments at shorter sample-to-detector distances, with the welcome effect of increased scattering intensity and the possibility to measure small-scale dynamics with increased structural sensitivity at larger q. The experimental setup may additionally be combined with specialized thin sample environments, such as microfluidics [132], for maximal benefit in terms of increased spatial resolution along the optical axis as well as speckle contrast.

Nevertheless, the use of nanobeams in XPCS does not come without challenges. These involve breakdown of usual assumptions that may not hold true for nanobeam sizes, for instance regarding the usually applicable neglect of number fluctuations [105] and beam divergence [133–135]. In *Paper II*, we present a first experimental demonstration of nano-XPCS where we highlight some of these challenges and suggest how to tackle them. In particular, we derive an analysis model (see below) that can account for the *large beam divergence* of nanofocused beams, which we observe cause a distortion in the small-angle scattering pattern as well as affect the measured dynamics.
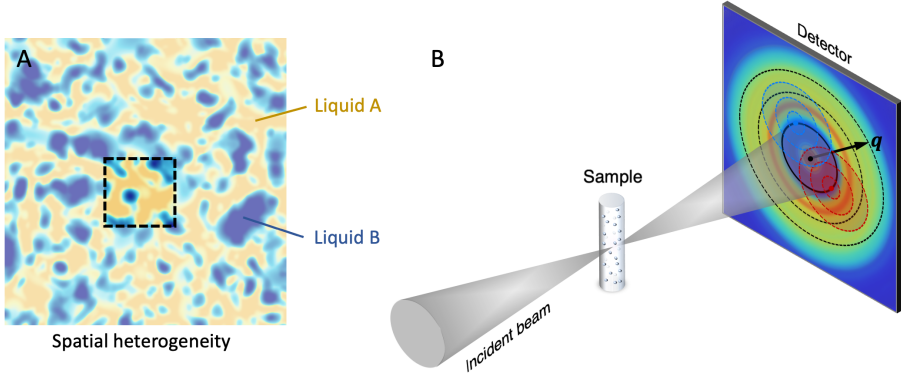
Figure 3.8: Nanofocused X-ray photon correlation spectroscopy (XPCS). (A) A nanofocused beam enhances sensitivity to spatial heterogeneities, e.g. in nanoscale heterogeneities in liquids, as indicated by the highlighted region. (B) A schematic illustrating the effect of large beam divergence on the scattering image in small-angle scattering geometry. The resulting scattering intensity I is a convolution of the divergent beam profile in the detector plane and the scattering intensity I_0 without divergence, as illustrated by the dashed circles where black refers to the scattering contributions from the beam center, similar to that from a beam with negligible divergence. Adapted from Ref. [128] with permission from the American Physical Society.

Explicitly, the measured scattered intensity I can be described mathematically as a convolution of the scattered intensity I_0, that would result from a beam with negligible divergence, with a point-spread function h, given by the divergent nanobeam profile projected onto the detector [134, 135] (see Fig. 3.8B). That is,

$$I = [I_0 * h](v) = \int I_0(u) \cdot h(v-u)\, du \,, \qquad (3.33)$$

where the notation $*$ indicates the mathematical operation of convolution, given on the right-hand side in its expanded form. For example, for a dilute nanoparticle solution I_0 would correspond to the particle form factor intensity $|F(q,R)|^2$. The resultant effect of a large beam divergence is generally a shifting and smearing out of the scattered intensity outwards from the hit of the direct beam, i.e. towards larger q. However, the distorting effects depend on the particular beam intensity profile, which may neither be round and nor homogeneous (see *Paper II*).

A similar effect of the beam divergence also influences the measured XPCS dynamics, i.e. the measured dynamic relaxation times τ (see *Paper II*). Normally, with negligible beam divergence, the relaxation time has a characteristic dependence on q, and thus on the radial distance from the beam center, such

as the typical $\tau^{-1} = Dq^2$ for diffusive dynamics. With large beam divergence though, the map of relaxation times as a function of the radial distance from the beam center gets distorted too, as a result of the convolution with the beam. As depicted schematically in Fig. 3.8B, the beam convolution can be described as a weighted average of the different scattering contributions (dashed circles) at each point in the scattering image. Here, the dashed circles denote a specific momentum transfer q value based on the concentric point of origin within the direct beam (solid black circle), which contribute with scattering intensity $I_0(q)$ and has a dynamic relaxation time $\tau_0(q)$, e.g. $\tau_0^{-1} = Dq^2$. The resulting relaxation times τ can therefore be expressed as a convolution of the relaxation time $\tau_0(q)$, weighted by the scattering intensity $I_0(q)$, with the point-spread function h:

$$\tau = (\tau_0 \cdot I_0) * h \, / \, (I_0 * h), \tag{3.34}$$

where the denominator is derived using integration by parts.

Lastly, a small scattering volume can also introduce additional dynamical effects, such as a significant contribution from number fluctuations, arising from scatterers entering and leaving the volume, that leads to breakdown of the Siegert relation (eq. (3.28)) [105, 136, 137]. Number fluctuations can generally be avoided though, as long as the average number of scatterers $\langle N \rangle$ within the scattering volume V is relatively large ($1/\langle N \rangle \ll 1$), or if the probed length scale is much smaller than the length scale of the scattering volume, i.e. $2\pi/q \ll V^{1/3}$ [105].

3.3 Generation of coherent X-rays

This section is intended to provide a basic understanding of different X-ray sources and generation of coherent X-rays. The descriptions are based on Ref. [138], unless referenced otherwise.

In standard X-ray tubes, which are used in conventional table-top X-ray diffraction (XRD) experiments, X-rays are generated by voltage-accelerated electrons hitting a metallic anode. As the electrons decelerate, they emit a continuous X-ray emission spectrum, called Bremsstrahlung radiation. In addition, collisions with the metal atoms cause inner electrons to be expelled. The subsequent relaxation of an outer shell electron into the hole, accompanied by the emission of a photon, gives rise to sharp X-ray emission lines. However, the natural randomness of the process, i.e. the X-ray emission is non-directed and unsynchronized in time, as well as efficiency limits, result in rather low X-ray coherence and intensity. Hence, such table-top X-ray sources cannot be used to resolve speckles, which require high coherent flux, and their application are therefore generally limited to measuring average or static scattering patterns. Instead, measuring dynamics from X-ray speckle patterns by XPCS requires the use of *coherent X-rays*, provided by *synchrotron X-ray radiation* or *X-ray free-electron lasers (XFELs)*.

An X-ray synchrotron radiation facility generally consists of four main parts: an electron source, a linear accelerator (LINAC), a booster ring and storage ring. From the electron source, the electrons are led into the LINAC where they are accelerated to extremely high speed. The electrons are further accelerated in a booster ring, after which they are injected into a final storage ring. Here, the highly energetic electrons (in the order of GeV) travel around in a large circle, their circular path being directed by the use of bending magnets. Inside the storage ring, the electrons pass through various components which, in addition to bending magnets, include series of alternating dipole magnets called wigglers and undulators, all of which generate X-ray radiation. Already the first generation of synchrotron radiation facilities produced X-rays with brilliance, a measure of coherent X-ray flux, about 6 orders of magnitude larger than the conventional table-top X-ray sources. Today, with the emergence of the fourth generation synchrotrons [139], like MAX IV Laboratory in Lund, Sweden [140], the brilliance is approaching that of XFELs, 20 orders of magnitude larger.

Synchrotron X-ray radiation is generated when a magnetic field forces an electron to arch its trajectory (i.e. the Lorentz force) and accelerate radially towards the center of the arc. The energy of the generated X-rays depends on the electron energy and on the magnitude of the magnetic field, while the X-ray power in addition depends on the length of the electron trajectory within the

magnetic field and on the current of electrons. Unlike bending magnets, where the electron path is bent only once, the series of alternating dipole magnets of wigglers and undulators provide a sinusoidal magnetic field, which forces the electrons to oscillate. The oscillatory electron motion, i.e. repeated bending of the electron trajectory, increases the total flux of the X-ray radiation. Increasing the number of oscillation periods results in a smaller angular divergence, a measure of how much the beam size increase with distance from the source, such that the generated X-ray beam becomes more collimated and directed. Undulators are longer than wigglers and the electrons oscillate with smaller amplitude, yielding a more collimated beam. This also produces a sharp line spectrum due to the interference of spatially overlapping X-ray waves.

In contrast to synchrotron radiation, which is considered a continuous X-ray source, XFELs produce a series of extremely intense and temporally short (in the order of femtoseconds) X-ray pulses. At XFELs, the X-rays are only generated in a LINAC, using a set of very long undulators. The use of these long undulators causes the radiated field from the oscillating electrons to eventually reach such strength that a process known as self-amplified spontaneous emission (SASE) is realized. In simple terms, the cloud of electrons travelling through the undulator start to respond to the electromagnetic field that is generated. The radiated field causes the large bunch of electrons to localize into smaller bunches. In turn, the spatially modulated electron bunches generate stronger radiation due to coherence and constructive interference, which modulates the electrons into even more compressed "micro-bunches". The feedback-loop finally saturates when the electron micro-bunches are separated spatially by the X-ray wavelength.

4. Summary of Results

4.1 Probing Nanoscale Fluctuations in Aqueous Solutions

The heart of thesis work commences in *Paper I*, where we investigate the character of the hypothesized HDL-LDL fluctuations in liquid water from the solute's perspective. Specifically, we study how these fluctuations manifest in solute diffusive dynamics, and explore the validity of the SE relation for solute diffusion in supercooled water, since its breakdown is hypothesized to originate from increasingly heterogeneous dynamics upon cooling [30, 32]. Using DLS (see Fig. 3.5), we measure the temperature-dependent diffusive dynamics for nanomolecular probes, from silica nanoparticles in the order of 100 nm to molecular-sized (≈ 1 nm) polyhydroxylated fullerenes (PHF), hypothesizing that the influence from water fluctuations, and the validity of the SE relation, may depend on the relative size of the probe and the spatial domains (see schematic in Fig. 4.1A).

However, independent of their size, we find that the probes display similar diffusive dynamics with an activation energy $E_A \approx 23$ kJ/mol, within the investigated temperature range ($260 - 300$ K). Moreover, using the SE relation, we extract the temperature-dependent viscosity experienced by the probes, and find that it is consistent with the macroscopic viscosity obtained from rheology. Thus, we find that the SE relation is preserved for all probes, down to molecular scales of ≈ 1 nm (see Fig. 4.1B). In contrast, the anomalously fast water self-diffusion upon supercooling (data from Ref. [144]) suggests that water molecules effectively experience lower viscosity, i.e. friction from their immediate surrounding, compared to the probes, resulting in breakdown of the SE relation. Based on the absence of size dependence in the diffusive dynamics, and the SE preservation, of the nanomolecular probes, we conclude that any critical probe size, below which probe dynamics is significantly influenced by water fluctuations, is likely on sub-nm length scales. Alternatively, the fluctuations do not significantly influence the probe dynamics on longer length scales ($\approx 0.1 - 1$ μm) related to the measurement q-range ($\approx 0.01 - 0.02$ nm^{-1}).

In *Paper II*, we develop a different experimental approach to capture liquid dynamics with sensitivity to nanoscale heterogeneities. Rather than using small particles as tracers of the surrounding liquid environment, we utilize the
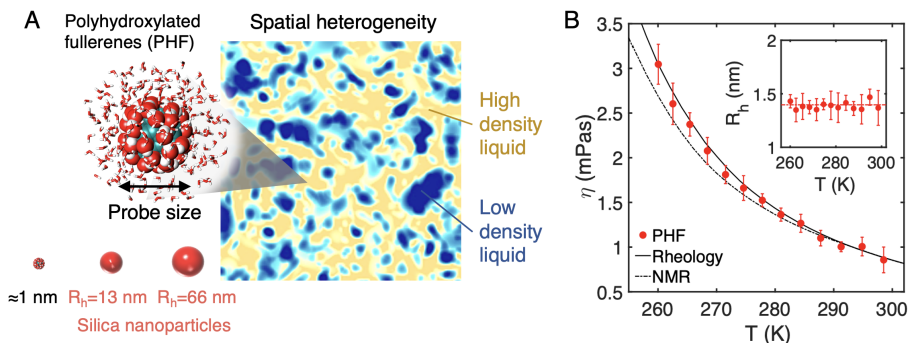
Figure 4.1: *Paper I*: Diffusive dynamics of nanomolecular probes in supercooled water. (A) A schematic illustrating the main idea behind the experiment; to explore the dependence on probe size in the diffusive dynamics of nanomolecular probes in supercooled water, which is hypothesized to be a fluctuating, spatially heterogeneous mixture of high- and low density liquid (HDL in yellow, LDL in blue). (B) The viscosity as a function of temperature. Red filled circles indicate the viscosity derived from dynamic light scattering measurements of the diffusion coefficient of polyhydroxylated fullerenes (PHF) that coincides with solid line indicating the macroscopic viscosity from rheology (Refs. [141–143]). In contrast, the viscosity derived from the self-diffusion of water molecules (Ref. [144]) is lower and increases more slowly upon supercooling (dashed line). The inset shows the effectively constant radius of PHF versus temperature, indicating preservation of the Stokes-Einstein relation within the temperature range. Reproduced from Ref. [13] with permission from the Royal Society of Chemistry.

spatial resolution of a small probing beam (see Fig. 3.8A). At the NanoMAX beamline at MAX IV [130, 145], the world's first 4th generation synchrotron radiation facility in Lund, Sweden [146], we conducted the first prototype experiment using nanofocused XPCS (nano-XPCS) for extracting dynamic information. The use of nanobeams (in the order of 100 nm) was combined with a state-of-the-art X-ray detector based on the Timepix3 chip [147, 148], allowing access to dynamics on microsecond and, potentially, even nanosecond time scales. Furthermore, the nano-XPCS experiments were carried out in SAXS geometry on prototypical nanoparticle suspensions (see schematic in Fig. 4.2A), and the effect of beam size on the measured dynamics was investigated by shifting the sample position along the optical axis of the divergent nanofocused beam.

We experimentally confirm that the use of nanobeams has the clear advantage of multi-fold increase in speckle contrast, which markedly improves signal-to-ratio (SNR), compared conventional micron-sized X-ray beams (see Fig. 4.2B). Nevertheless, comparison with theoretical models indicates that there is still substantial room for contrast improvement by minimizing the sam-
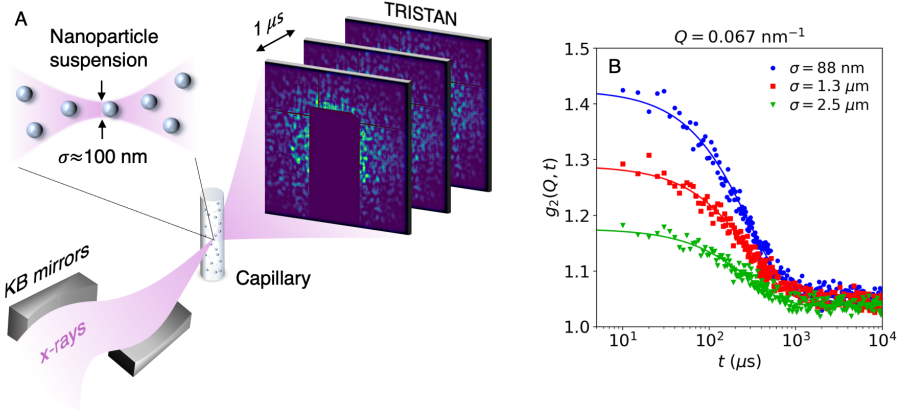
Figure 4.2: *Paper II*: Experimental demonstration of nanofocused X-ray photon correlation spectroscopy (nano-XPCS). (A) A schematic overview of the nano-XPCS experiment carried out at the NanoMAX beamline at MAX IV. Dynamics of nanoparticle suspensions were measured in small-angle scattering (SAXS) geometry with a nanofocused X-ray beam (beam size $\sigma \approx 100$ nm) and microsecond resolution using the state-of-the-art Tristan detector. (B) The use of X-ray nanobeams results in strongly increased speckle contrast as demonstrated here in the intercept of the measured autocorrelation function g_2 of nanoparticle suspensions as a function of beam size σ. Reprinted from Ref. [128] with permission from the American Physical Society.

ple thickness (1 mm in the current experiment) along the optical axis, which would also maximize the spatial resolution. Furthermore, we show how the large angular divergence of nanofocused beams affects the SAXS lineshape and the measured diffusive dynamics, and demonstrate how these effects can be accounted for by deriving an analytical model involving a convolution with the divergent beam. We hypothesize that the influence of the beam divergence can be minimized by measuring at larger momentum transfer q, taking advantage of the increased contrast from nanobeams and emerging X-ray detector technologies, that allow to measure faster dynamics. In conclusion, the results in *Paper II* experimentally demonstrate the combination of coherent X-ray nanobeams with XPCS, and its promising potential for resolving spatially heterogeneous dynamics.

4.2 Resolving Liquid-Liquid Transitions in Aqueous Solutions

In *Paper I*, we studied the influence of water fluctuations on solutes. Continuing these investigations in *Paper III-IV*, we look instead from the perspec-
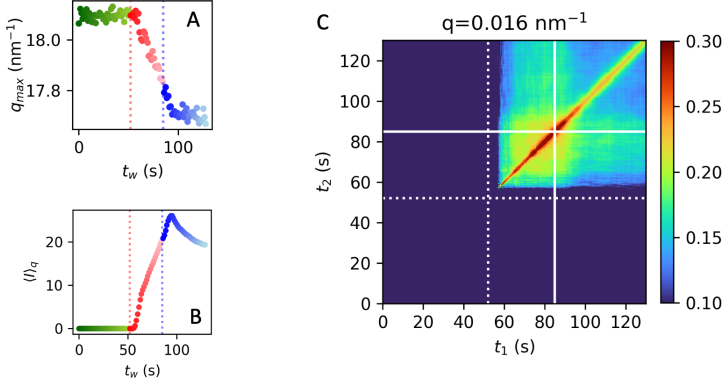
Figure 4.3: *Paper III*: Indications of a first-order like liquid-liquid transition (LLT) in deeply supercooled 16.5 mol% glycerol-water solution after quenching to $T = 172 \pm 4$ K. (A) The peak position q_{max} from wide-angle X-ray scattering (WAXS) and (B) the enhancement of the average ultra small-angle X-ray scattering (USAXS) intensity $\langle I \rangle_q$ ($0.01 \leq q \leq 0.2$ nm^{-1}) as a function of waiting time t_w. The different coloring indicate three stages of liquid transformation; initial liquid state (green), rapidly changing liquid structure during an LLT (red), and formation of ice crystallites (blue). (C) The TTC function showing the advent of a TTC signal coincident with the rapid changes in the WAXS and USAXS. Here, delay times t_1 and t_2 both relate to the waiting time t_w and the white dotted and solid lines indicate the onset of USAXS enhancement and ice crystallization. The temporal evolution of the dynamics as a function the waiting time can be followed along the TTC diagonal (where $t_1 = t_2$). Reprinted from *Paper III (manuscript)*.

tive of water and investigate how the addition of solutes modulates the HDL-LDL transitions in the phase diagram. Using binary solutions of water and the small polar-organic cryoprotectant molecule glycerol as model system, we explore the solution structure and dynamics within the supercooled regime of the glycerol-water phase diagram.

In *Paper III*, we investigate supercooled glycerol-water solutions at intermediate glycerol concentrations (16.5 mol%) by conducting synchrotron experiments at PETRA III (DESY). Here, we combine XPCS in the ultrasmall angle scattering (USAXS) range and WAXS, allowing us to simultaneously acquire dynamical information at nanometer length scales and monitor the changes in the liquid inter-atomic structure, such as ice crystallization. Following quenching (moderate cooling rate 20 K/min) of the solution to $T = 172 \pm 4$ K, we observe a sudden and rapid shift of the liquid peak position in WAXS towards lower q (red-colored range, Fig. 4.3A), prior to the onset of ice crystallization (blue-colored range, Fig. 4.3A). The latter is evident from the subsequent appearance of ice bragg peaks in the WAXS pat-

tern, indicating formation of ice crystallites. Concurrent with the changes in the inter-atomic liquid structure, there is a strong enhancement of the USAXS intensity indicating micro-scale heterogenieties (Fig. 4.3B), as well as a discontinuous emergence of a TTC signal (Fig.4.3C). We interpret these observations, in particular the discontinuous nature of the transition in the structure and dynamics, as indications of a first-order-like LLT, preceding ice crystallite formation. Analysis of the TTC allows to follow the temporal evolution of the nanoscale dynamics during the initial LLT stage, before freezing, which reveals a gradual slowdown. In addition, the dynamics exhibit characteristics of ballistic-like super-diffusive motion, consistent with an LLT via spinodal decomposition (SD) [113, 114]. We conclude that our results indeed are in line with the hypothesis of a liquid-liquid phase coexistence line at ambient pressure in deeply supercooled glycerol-water solutions at intermediate glycerol concentrations [75].

In contrast to intermediate glycerol concentration, the supercooled regime of dilute glycerol-water solutions is vastly unexplored and inaccessible due to freezing. To experimentally access the dilute supercooled regime, we utilize in *Paper IV* the rapid evaporative cooling approach combined with ultrafast X-ray scattering at SACLA XFEL (see Fig. 4.4A). In this approach, microdroplets (18.7 μm diameter) of the dilute solution (3.2 mol% glycerol-water) are rapidly cooled by evaporation in vacuum, which allows to outrun ice nucleation and reach temperatures down to $T \approx 229$ K in the deeply supercooled regime. The instantaneous droplet temperature depends on the evaporation time (millisecond time scales), i.e. on the travel distance from the droplet dispenser (Fig. 4.4A). Since the probability that the droplets freeze is significant at lower temperature, some droplets remain in the metastable liquid state while others freeze. Thus, to selectively capture the supercooled liquid state there is a need to use ultrafast probing. The use of intense femtosecond XFEL pulses allows to record X-ray scattering patterns of the microdroplets on a single-shot basis (i.e. one XFEL pulse is used to generate a scattering pattern from a single droplet), and recordings from frozen droplets (evident from the ice bragg peaks in WAXS) can be discarded in the post-analysis [9, 21]. In this experiment, we additionally use a large-area detector to capture the WAXS and SAXS range simultaneously, allowing us to observe the local liquid structure as well as density fluctuations. We further complement the X-ray scattering experiments with MD simulations of the glycerol-water system.

From the experimental results in *Paper IV*, we observe that the first structure factor peak position S_1 (from WAXS) of 3.2 mol% glycerol-water solution shifts towards lower momentum transfer q upon cooling (see Fig. 4.4B). This trend is consistent with our complementary MD simulations, as well as with similar experiments on pure water [9], where the shift indicates a higher
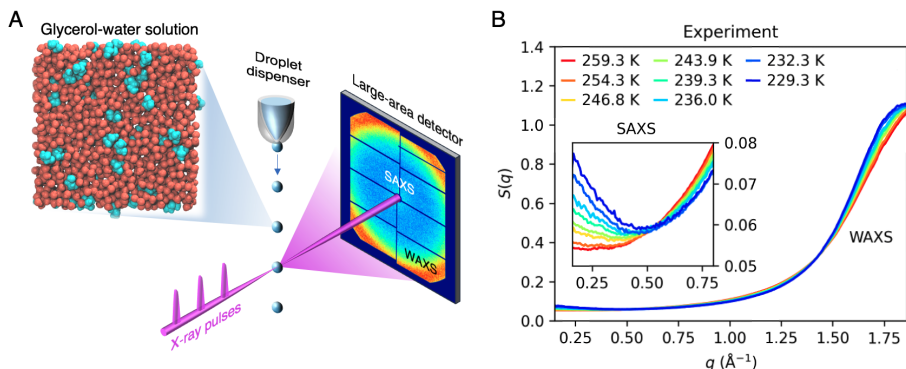
Figure 4.4: *Paper IV*: Capturing the structure factor of deeply supercooled 3.2 mol% glycerol-water. (A) A schematic of the experiment carried out at SACLA X-ray free-electron laser (XFEL). 18.7-μm sized droplets of 3.2 mol% glycerol-water solution are evaporatively cooled and probed by small- and wide-angle X-ray scattering (SAXS, WAXS) using ultrashort X-ray pulses. (B) The scattering patterns of evaporatively supercooled 3.2 mol% glycerol-water solution at different temperatures, over a *q*-range from SAXS to WAXS. The inset highlights the strong enhancement of the SAXS intensity upon supercooling. Reprinted from *Paper IV (manuscript)*.

degree of tetrahedral coordination associated with more LDL at lower temperatures [9, 21, 149]. An increase of LDL-like water in the supercooled glycerol-water solution is additionally supported by analysis of the local structure index (LSI) in the MD simulations, which indicate that the average LSI per water molecule increases upon cooling. In the experimental results, we further observe enhancement of the SAXS signal upon supercooling (Fig. 4.4B inset), indicative of increasing density fluctuations. Similar to pure water [97], the isothermal compressibility κ_T extracted from analysis of the SAXS signal increases monotonically with a power-law like behaviour within the experimental temperature range ($T \gtrsim 229$ K). Below the experimental range, the MD simulations suggest the existence of an isothermal compressibility maximum at $T_{max} \approx 220$ K, indicating the location of a Widom line at ambient pressure, slightly shifted to lower temperature compared to pure bulk water [9, 97].

5. Conclusions and Outlook

In this thesis, we have explored the role of molecular heterogeneities in the structural dynamics of aqueous solutions, using the coherent properties of visible lasers and X-rays. We have presented experimental investigations on the relation between the LLCP hypothesis of water, that predicts local fluctuations between HDL and LDL, and the presence of solutes in aqueous solutions. In addition, we have made significant progress in the method development of XPCS for extracting structural dynamic information, in particular nanoscale fluctuations, utilizing the increase of coherence at the new DLSRs, such as MAXIV synchrotron radiation facility in Lund, Sweden. The results presented herein contribute to our fundamental understanding of the properties of water, and its unique and essential role as a solvent in nature and for living processes.

So what have we learned? While more experimental and simulation studies in recent years present evidence that support the LLCP hypothesis of water [9–12, 22–24, 28], little is known about its impact on the structure and dynamics of aqueous solutions. Herein, we explored the influence of the hypothesized HDL-LDL fluctuations on the dynamics of differently sized nanomolecular probes in dilute supercooled aqueous solutions (*Paper I*). In contrast to the self-diffusion of water molecules, our findings indicate that the diffusive dynamic behaviour of the probes preserves the Stokes-Einstein relation, independent of the probe size down to molecular scales of ≈ 1 nm. These results for ambient temperature to moderate supercooling ($T \geq 260$ K) may suggest that the hypothesized water fluctuations mainly influence dynamics on sub-nm length scales. While collective nano- to macro scale solute dynamics might be less affected, it does not exclude the possibility of the fluctuations having substantial effects on atomic to molecular dynamics, such as intramolecular motions involved in chemical or biomolecular reactions and processes. Moroever, our experiments on deeply supercooled glycerol-water solutions indicate that HDL- and LDL-like liquids and their fluctuations can be vividly present and significantly affect the solution behavior (*Paper III, IV*).

Using rapid evaporative cooling and ultrafast X-ray scattering at SACLA XFEL, we probed the liquid structure of dilute glycerol-water solution (3.2 mol%) below the homogenous nucleation limit (*Paper IV*). Here, we measured a strong enhancement of the SAXS intensity and the isothermal compressibility. Simultaneously, the shift of the first structure factor peak in WAXS to lower

momentum transfer q upon supercooling can be related to increased tetrahedral coordination, associated more LDL-like liquid. Hence, the enhancements could indicate the increase in HDL- and LDL-like fluctuations in the vicinity of a Widom line present in these aqueous solutions. Our complementary MD simulations support these experimental observations and further predicts a shift of the Widom line location to lower temperatures. Moreover, we measured glycerol-water solutions at higher glycerol concentrations (16.5 mol%) in synchrotron radiation experiments performed at PETRA III, DESY (*Paper III*). In these experiments, we were able to temporally resolve discontinuous liquid structural transformations in WAXS and USAXS, as well as dynamics from XPCS, in the deeply supercooled regime. Our observations here are consistent with a first-order-like LLT at ambient pressure, where the LLT precedes the onset ice crystallization. Combined, the findings from our investigations of glycerol-water solutions suggest that glycerol molecules influence the local structure of the hydrogen-bond network of water in a way similar to pressure. Thus, the location of a possible LLCP in these solutions may be accessible by exploring several different glycerol concentrations. In any case, these results support the relevance of HDL- and LDL-like water fluctuations in aqueous solutions and their supercooled phase behavior. The latter can be of particular practical importance for cryopreservation of biological material, which often utilizes aqueous solutions of cryoprotectants, such as glycerol, to suppress freezing [60, 74, 150].

To resolve the origin of the anomalous properties of water, the development of experimental techniques has proved crucial [9–12, 21, 37]. In this work, we have taken additional steps to shed light on the behaviour aqueous solutions, in which nanoscale spatial fluctuations could play an important role while their relation to the complex structural dynamics remains to be better understood. Through our prototype experiment performed at NanoMAX synchrotron beamline, MAXIV, we successfully demonstrated experimentally for the first time the use of nanofocused XPCS for measuring structural dynamics (*Paper II*). We showed that the use of this technique has the potential to resolve nanoscale fluctuations in solutions and other systems across fields. Furthermore, combining the gain in speckle contrast and spatial resolution from nanofocused X-ray beams with novel detector technologies, could potentially provide access to vastly unexplored atomic- to nanoscale dynamics on micro- to nanosecond time scales. A strategic next step in the development of XPCS in these directions would be to conduct nanofocused XPCS experiments on samples with thin sample thickness, thereby maximize the gain in speckle contrast, and at larger momentum transfer q, which targets smaller length scales and where the influence from the nanobeam divergence should be less pronounced.

Looking ahead to future investigations, we are expanding on our capabilities towards accessing atomic-scale liquid dynamics on picosecond time scales. These dynamics, which can give insights into dynamic heterogeneities such as cage effects, can be accessed by X-ray speckle visibility spectroscopy (XSVS) which utilizes the high degree of coherence and ultrashort X-ray pulses of XFELs [37, 120, 151]. In this case, the decay of the speckle contrast (visibility) recorded from a pair of XFEL pulses, as a function of the picosecond pulse separation, is used to directly measure the intermediate scattering function in the time domain. Previous experimental attempts of this technique has suffered from weak scattering intensity from the sample, and from low speckle contrast from angular mismatch between the two pulses [152–154]. To tackle these issues, we are planning to perform an XSVS experiment to measure the dynamics in DMSO-water solutions, utilizing instead the new amplitude-splitting method recently available at LCLS XFEL, US. Here, the presence of DMSO will contribute to increasing scattering intensity due to the higher scattering power of the sulphur atom compared to pure water, as tested previously [37, 154]. These efforts will lay the foundation for future XSVS experiments to resolve ultrafast molecular dynamics, which may hold important clues to understanding structural dynamics in aqueous solutions and other complex liquids.

Populärvetenskaplig sammanfattning

Vatten är en livsnödvändig vätska, men det har länge saknats en fullständig förklaring till vattens många underliga egenskaper, till exempel dess densitetsmaximum vid 4°C. Enligt en teori kan vatten existera i två flytande tillstånd - så kallad högdensitets- och lågdensitetsvätska (HDL, LDL). Vid normalt atmosfärstryck spår man att vatten fluktuerar mellan dessa två tillstånd, och ju kallare vattnet är, desto mer intensiva blir fluktuationerna. För att bevisa hypotesen krävs dock avancerade experimentella mätningar av flytande vatten kylt under frystpunkten, så kallat underkylt vatten.

Om de förutspådda vattenfluktuationerna existerar kan de ha stor inverkan på hur vatten interagerar med andra ämnen, inte minst i biologiska processer som i stort sett sker i vattenlösning. I den här forskningsavhandlingen utforskar vi hur små variationer i molekylär sammansättning kan påverka vattnets beteende, samt hur olika lösningsämnen interagerar med vatten och med de förmodade vattenfluktuationerna. För att göra detta använder vi avancerad teknik såsom koherent ljus- och röntgenspridning, som gör det möjligt att studera vätskans struktur och strukturella dynamik på mikroskopiska längdskalor.

Med dynamisk ljusspridning (DLS) följer vi hur molekyler och nanopartiklar diffunderar i underkylt vatten. Förvånansvärt nog verkar partiklarna känna av en liknande dynamisk omgivning när de rör sig i vattnet, oavsett partiklarnas storlek. Detta kan antyda att de hypotetiska vattenfluktuationerna främst influerar lösningsämnen på mindre, atomära längdskalor. Vi granskar också hur närvaron av små organiska molekyler påverkar vattnets beteende, och använder oss av glycerol-vattenlösningar som ett modellsystem. Genom ultrasnabb röntgenspridning vid röntgen-fri-elektronlasrar (X-ray free-electron lasers, XFELs), kan vi studera hur vätskestrukturen förändras vid extrem underkylning. Våra resultat antyder att det existerar fluktuationer liknande HDL och LDL även i vatten blandat med andra ämnen, alltså inte enbart i rent vatten.

Slutligen, med målet att utveckla kraftfulla verktyg för att förstå den strukturella dynamiken i komplexa system, inklusive vattenlösningar, utför vi experiment som för första gången kombinerar nanofokuserade röntgenstrålar med dynamiska mätningar genom så kallad röntgen-foton-korrelationsspektroskopi (X-ray photon correlation spectroscopy, XPCS). Genom att använda denna teknik kan vi utforska fluktuationer i vätskestrukturen på nanometerskala och dess betydelse för vätskors komplexa beteende. Detta arbeta lägger grunden för en fortsatt spännande resa mot att förstå vattnets mysterier, likväl som vattnets roll som livsviktig vätska i biologiska system, på molekylär nivå.

Acknowledgements

First and foremost, I would like to sincerely thank my supervisor Fivos Perakis. Thank you for your guidance, kindness, patience and encouragement. I have very much enjoyed our scientific discussions. Especially, I want to say thanks for being so open and inclusive, encouraging me and the rest of the group to think creatively and to express our ideas. I have truly learned a lot from you in many aspects during this time, for which I am immensely grateful.

Furthermore, I want to give special thanks to current and former members of the Structural Dynamics of Aqueous Solutions (SDAqS) team. Your support and high spirits have been crucial to the success of this work. The synchrotron radiation and XFEL experiments could not have been done without your excellent help. It has been a pleasure to work with such a skillful team of people.

Maddalena, I am grateful to have had you as a colleague throughout all these years. Already from the start I was impressed by your excellent work and eagerness to learn. Sudipta, thank you for your diligent support during the early years of my PhD. Mario, we (and I) would not have survived without your superior programming and data analysis skills. Mariia, I admire your versatility, experimental skills and organization. Your support has been really valuable and reassuring. Anita, it has been a pleasure working with you this last year. Thank you for all your kind help and the joy you bring to the group. Iason, I have no doubts that you are going to do great in the coming years of your PhD. It has been a pleasure to collaborate with you, and I am really impressed by your already very skillful work. In addition to all the hard work, I will also remember the adventures of travelling abroad for beamtimes around the world. Thankfully our team was complementary, with early birds (me) and night owls (definitely not me), making these beamtime experiences a lot more pleasant with a good night's sleep. Maddalena, Mariia and Anita, thank you for keeping up with my vacation pace in Japan and for not letting the aggressive monkeys catch us in the Japanese forest.

Moreover, I would like to acknowledge the rest of the XSoLaS group. Thank you for providing such a kind and open atmosphere. Special thanks to Aigerim, it has been really nice and comforting to have someone as kind and humble as you to share the PhD journey with from start to end. Marjorie, you have really been a pillar throughout this time. In addition to science, we found a lot of shared interests and I am happy to see the growth of our friendship over

these years. Thank you to co-supervisor Tony, for first introducing me to the division during our work together on my master's thesis, which I truly enjoyed a lot. Anders (co-supervisor) and Lars, thank you for all the feedback over the years, and for so pedagogically sharing your solid experience and helping with data interpretation. In addition, I would also like to thank people from the technical division for help and support, not least Petra and Matthias whom I worked more closely with.

Last and not least, I wish to express my deepest gratitude to my close family and friends, who have supported me during all this time. MMichael, thank you so much for putting up with all my sighs of struggle and for putting things in perspective. And finally, my beloved grandfather "Sabba Uzi", I want to thank you especially for always taking such an interest in my work. Your curiosity about science has been inspiring me from the start.

References

1. Oh, K.-I. & Baiz, C. R. Molecular heterogeneity in aqueous cosolvent systems. *J. Chem. Phys.* **152,** 190901 (2020).

2. Oh, K. I., You, X., Flanagan, J. C. & Baiz, C. R. Liquid-Liquid Phase Separation Produces Fast H-Bond Dynamics in DMSO-Water Mixtures. *J. Phys. Chem. Lett.* **11,** 1903 (2020).

3. Perakis, F. & Gutt, C. Towards molecular movies with X-ray photon correlation spectroscopy. *Phys. Chem. Chem. Phys.* **22,** 19443 (2020).

4. Atkins, P. & de Paula, J. in *Atkins' Physical Chemistry* 8th ed., 136–173 (W. H. Freeman and Company, 2006).

5. Shin, Y. & Brangwynne, C. P. Liquid phase condensation in cell physiology and disease. *Science* **357,** eaaf4382 (2017).

6. Debenedetti, P. G. Supercooled and glassy water. *J. Phys.: Condens. Matter* **15,** R1669 (2003).

7. Debenedetti, P. G. & Stillinger, F. H. Supercooled liquids and the glass transition. *Nature* **410,** 259 (2001).

8. Nilsson, A. & Pettersson, L. G. The structural origin of anomalous properties of liquid water. *Nature Communications* **6,** 8998 (2015).

9. Kim, K. H. *et al.* Maxima in the thermodynamic response and correlation functions of deeply supercooled water. *Science* **358,** 1589 (2017).

10. Kim, K. H. *et al.* Experimental observation of the liquid-liquid transition in bulk supercooled water under pressure. *Science* **370,** 978 (2020).

11. Pathak, H. *et al.* Enhancement and maximum in the isobaric specific-heat capacity measurements of deeply supercooled water using ultrafast calorimetry. *PNAS* **118,** e2018379118 (2021).

12. Perakis, F. *et al.* Diffusive dynamics during the high-To-low density transition in amorphous ice. *Proc. Natl. Acad. Sci. U.S.A* **114,** 8193 (2017).

13. Berkowicz, S. & Perakis, F. Exploring the validity of the Stokes–Einstein relation in supercooled water using nanomolecular probes. *Phys. Chem. Chem. Phys.* **23,** 25490 (2021).

14. Dubey, V., Dueby, S., Erimban, S. & Daschakraborty, S. Importance of Translational Jump in Diffusion of Hydrophobic Solute in Supercooled Water: Solute Size Dependence. *J. Indian Chem. Soc.* **96,** 741 (2019).

15. Bin, M. *et al.* Wide-angle X-ray scattering and molecular dynamics simulations of supercooled protein hydration water. *Phys. Chem. Chem. Phys.* **23,** 18308 (2021).

16. Poole, P. H., Sciortino, F., Essmann, U. & Stanley, H. E. Phase behaviour of metastable water. *Nature* **360,** 324 (1992).

17. M. Chaplin. *Water data (supplementary)* www.water.lsbu.ac.uk. https://water.lsbu.ac.uk/water/data1.html (2022).

18. Speedy, R. J. & Angell, C. A. Isothermal compressibility of supercooled water and evidence for a thermodynamic singularity at 45°C. *J. Chem. Phys.* **65,** 851 (1976).

19. Johari, G. P., Hallbrucker, A. & Mayer, E. The glass–liquid transition of hyperquenched water. *Nature* **330,** 552 (1987).

20. Langham, E. J., Mason, B. J. .-. N. & Bernal, J. D. The heterogeneous and homogeneous nucleation of supercooled water. *Proc. R. Soc. Lond. A* **247,** 493 (1958).

21. Sellberg, J. A. *et al.* Ultrafast X-ray probing of water structure below the homogeneous ice nucleation temperature. *Nature* **510,** 381 (2014).

22. Jeffrey R. Errington & Pablo G. Debenedetti. Relationship between structural order and the anomalies of liquid water. *Nature* **409,** 318 (2001).

23. Palmer, J. C. *et al.* Metastable liquid–liquid transition in a molecular model of water. *Nature* **510,** 385 (2014).

24. Debenedetti, P. G., Sciortino, F. & Zerze, G. H. Second critical point in two realistic models of water. *Science* **369,** 289 (2020).

25. Mishima, O., Calvert, L. D. & Whalley, E. An apparently first-order transition between two amorphous phases of ice induced by pressure. *Nature* **314,** 76 (1985).

26. Mishima, O. & Stanley, H. E. The relationship between liquid, supercooled and glassy water. *Nature* **396,** 329 (1998).

27. Xu, L. *et al.* Relation between the Widom line and the dynamic crossover in systems with a liquid-liquid phase transition. *Proc. Natl. Acad. Sci. U.S.A.* **102,** 16558 (2005).

28. Nilsson, A. Origin of the anomalous properties in supercooled water based on experimental probing inside "no-man's land". *J. Non-Cryst.* **14,** 100095 (2022).

29. Ito, K., Moynihan, C. T. & Angell, C. A. Thermodynamic determination of fragility in liquids and a fragile-to-strong liquid transition in water. *Nature* **398,** 492 (1999).

30. Shi, R., Russo, J. & Tanaka, H. Origin of the emergent fragile-to-strong transition in supercooled water. *Proc. Natl. Acad. Sci. U.S.A.* **115,** 9444 (2018).

31. Chen, S.-H. *et al.* The Violation of the Stokes-Einstein Relation in Supercooled Water. *Proc. Natl. Acad. Sci. U.S.A.* **103,** 12974 (2006).

32. Dehaoui, A., Issenmann, B. & Caupin, F. Viscosity of deeply supercooled Water and its coupling to molecular diffusion. *Proc. Natl. Acad. Sci. U.S.A.* **112,** 12020 (2015).

33. Kawasaki, T. & Kim, K. Identifying time scales for violation/preservation of Stokes-Einstein relation in supercooled water. *Sci. Adv.* **3,** 1 (2017).

34. Laage, D. & Hynes, J. T. A Molecular Jump Mechanism of Water Reorientation. *Science* **311,** 832 (2006).

35. Dueby, S., Dubey, V. & Daschakraborty, S. Decoupling of Translational Diffusion from the Viscosity of Supercooled Water: Role of Translational Jump Diffusion. *J. Phys. Chem. B* **123,** 7178 (2019).

36. Dubey, V., Erimban, S., Indra, S. & Daschakraborty, S. Understanding the Origin of the Breakdown of the Stokes-Einstein Relation in Supercooled Water at Different Temperature-Pressure Conditions. *J. Phys. Chem. B* **123,** 10089 (2019).

37. Perakis, F. *et al.* Coherent X-rays reveal the influence of cage effects on ultrafast water dynamics. *Nature Communications* **9,** 1917 (2018).

38. Clayden, J., Greeves, N. & Warren, S. *Organic chemistry* 2nd ed. (Oxford University Press Inc., 2012).

39. Ianiro, A. *et al.* Liquid-liquid phase separation during amphiphilic self-assembly. *Nat. Chem.* **11,** 320.

40. Campbell, M. K. & Farrell, S. O. in *Biochemistry* 7th ed., 193–226 (Brooks/Cole, Cengage Learning, 2012).

41. Levy, Y. & Onuchic, J. N. Water mediation in protein folding and molecular recognition. *Annu. Rev. Biophys. Biomol. Struct.* **35,** 389 (2006).

42. Biedermannová, L. & Schneider, B. Hydration of proteins and nucleic acids: Advances in experiment and theory. A review. *Biochimica et Biophysica Acta* **1860,** 1821 (2016).

43. Campbell, M. K. & Farrell, S. O. in *Biochemistry* 7th ed., 165–192 (Brooks/Cole, Cengage Learning, 2012).

44. Garczarek, F. & Gerwert, K. Functional waters in intraprotein proton transfer monitored by FTIR difference spectroscopy. *Nature* **439,** 109 (2006).

45. R. Mancinelli, A. Botti, F. Bruni, M. A. Ricci & A. K. Soper. Hydration of Sodium, Potassium, and Chloride Ions in Solution and the Concept of Structure Maker/Breaker. *J. Phys. Chem.* **111,** 13570 (2007).

46. Marcus, Y. Effect of Ions on the Structure of Water: Structure Making and Breaking. *Chem. Rev.* **109,** 1346 (2009).

47. Chen, Y. *et al.* Electrolytes induce long-range orientational order and free energy changes in the H-bond network of bulk water. *Sci. Adv.* **2,** e1501891.

48. Murata, K.-i. & Tanaka, H. General nature of liquid–liquid transition in aqueous organic solutions. *Nat. Commun.* **4,** 2844 (2013).

49. Yagasaki, T., Matsumoto, M. & Tanaka, H. Liquid-liquid separation of aqueous solutions: A molecular dynamics study. *The Journal of Chemical Physics* **150,** 214506 (2019).

50. Suzuki, Y. Direct observation of reversible liquid–liquid transition in a trehalose aqueous solution. *Proceedings of the National Academy of Sciences* **119,** e2113411119 (2022).

51. Perets, E. A. & Yan, E. C. Y. The H2O Helix: The Chiral Water Superstructure Surrounding DNA. *ACS Cent. Sci.* **3,** 683 (2017).

52. Perets, E. A. & Yan, E. C. Y. Chiral Water Superstructures around Antiparallel -Sheets Observed by Chiral Vibrational Sum Frequency Generation Spectroscopy. *J. Phys. Chem. Lett.* **10,** 3395 (2019).

53. Suzuki, Y. Effect of OH groups on the polyamorphic transition of polyol aqueous solutions. *J. Chem. Phys.* **150,** 224508 (2019).

54. Mallamace, F., Mallamace, D., Chen, S.-H., Lanzafame, P. & Papanikolaou, G. Hydrophilic and Hydrophobic Effects on the Structure and Themodynamic Properties of Confined Water: Water in Solutions. *Int. J. Mol. Sci.* **22,** 7547 (2021).

55. Corradini, D., Su, Z., Stanley, H. E. & Gallo, P. A molecular dynamics study of the equation of state and the structure of supercooled aqueous solutions of methanol. *J. Chem. Phys.* **137,** 184503 (2012).

56. Juurinen, I. *et al.* Effect of the Hydrophobic Alcohol Chain Length on the Hydrogen-Bond Network of Water. *J. Phys. Chem. B* **118,** 39 (2014).

57. Perera, A. & Mazighi, R. On the nature of the molecular ordering of water in aqueous DMSO mixtures. *J. Chem. Phys* **143,** 154502 (2015).

58. Lotze, S., Groot, C. C. M., Vennehaug, C. & Bakker, H. J. Femtosecond Mid-Infrared Study of the Dynamics of Water Molecules in Water–Acetone and Water–Dimethyl Sulfoxide Mixtures. *J. Phys. Chem. B* **119,** 5228 (2015).

59. McLain, S. E., Soper, A. K., Luzar, A. & Investigations, A. Investigations on the structure of dimethyl sulfoxide and acetone in aqueous solution. *J. Phys. Chem.* **127,** 174515 (2007).

60. Ghosh, N., Roy, S., Ahmed, M. & Mondal, J. A. Water in the hydration shell of cryoprotectants and their non-cryoprotecting structural analogues as observed by Raman-MCR spectroscopy. *J. Mol. Liq.* **266,** 188 (2018).

61. Laage, D., Stirnemann, G., Sterpone, F., Rey, R. & Hynes, J. T. Reorientation and Allied Dynamics in Water and Aqueous Solutions. *Annu. Rev. Phys. Chem.* **62,** 395 (2011).

62. Fogarty, A. C., Duboué-Dijon, E., Sterpone, F., Hynes, J. T. & Laage, D. Biomolecular hydration dynamics: a jump model perspective. *Chem. Soc. Rev.* **42,** 5672 (2013).

63. Kumar, P. *et al.* Glass transition in biomolecules and the liquid-liquid critical point of water. *Phys. Rev. Lett.* **97,** 177802 (2006).

64. Chen, S.-H. *et al.* Observation of fragile-to-strong dynamic crossover in protein hydration water. *Proc. Natl. Acad. Sci. U.S.A.* **103,** 9012 (2006).

65. Kokubo, K., Matsubayashi, K., Tategaki, H., Takada, H. & Oshima, T. Facile Synthesis of Highly Water-Soluble Fullerenes More Than Half-Covered by Hydroxyl Groups. *ACS Nano* **2,** 327 (2008).

66. Kokubo, K., Shirakawa, S., Kobayashi, N., Aoshima, H. & Oshima, T. Facile and scalable synthesis of a highly hydroxylated water-soluble fullerenol as a single nanoparticle. *Nano Res.* **4,** 204–215 (2011).

67. Chaban, V. V. & Fileti, E. E. Which fullerenols are water soluble? Systematic atomistic investigation. *New J. Chem.* **41,** 184 (2016).

68. Vraneš, M. *et al.* Self-assembling, reactivity and molecular dynamics of fullerenol nanoparticles. *Phys. Chem. Chem. Phys.* **19,** 135 (2017).

69. MacIel, C., Fileti, E. E. & Rivelino, R. Assessing the solvation mechanism of C60(OH)24 in aqueous solution. *Chem. Phys. Lett.* **507,** 244 (2011).

70. Semenov, K. N. *et al.* Fullerenols: Physicochemical properties and applications. *Prog. Solid. State Ch.* **44,** 59 (2016).

71. Cupane, A., Fomina, M., Piazza, I., Peters, J. & Schirò, G. Experimental Evidence for a Liquid-Liquid Crossover in Deeply Cooled Confined Water. *Phys. Rev. Lett.* **113,** 215701 (2014).

72. Oguni, M., Kanke, Y., Nagoe, A. & Namba, S. Calorimetric Study of Waters Glass Transition in Nanoscale Confinement, Suggesting a Value of 210 K for Bulk Water. *J. Phys. Chem. B* **115,** 14023 (2011).

73. Nagoe, A., Kanke, Y., Oguni, M. & Namba, S. Findings of Cp Maximum at 233 K for the Water within Silica Nanopores and Very Weak Dependence of the Tmax on the Pore Size. *J. Phys. Chem. B* **114,** 13940 (2010).

74. Yoshimura, Y., Ishikawa, Y. & Takekiyo, T. Cryopreservation of proteins in aqueous DMSO solutions at cryogenic temperature: A case study of lysozyme. *J. Mol. Liq.* **273,** 663 (2019).

75. Murata, K.-i. & Tanaka, H. Liquid–liquid transition without macroscopic phase separation in a water–glycerol mixture. *Nat. Mater.* **11,** 436 (2012).

76. Bachler, J. *et al.* Glass polymorphism in glycerol–water mixtures: II. Experimental studies. *Phys. Chem. Chem. Phys.* **18,** 11058–11068 (2016).

77. Huerta-Viga, A. *et al.* Glass formation of a DMSO-water mixture probed with a photosynthetic pigment. *Phys. Chem. Chem. Phys.* **20,** 17552 (2018).

78. Rasmussen, D. H. & MacKenzie, A. P. Phase Diagram for the System Water-Dimethylsulphoxide. *Nature* **220,** 1315 (1968).

79. Woutersen, S., Ensing, B., Hilbers, M., Zhao, Z. & Angell, C. A. A liquid-liquid transition in supercooled aqueous solution related to the HDA-LDA transition. *Science* **359,** 1127–1131 (2018).

80. Corradini, D. & Gallo, P. Liquid–Liquid Coexistence in NaCl Aqueous Solutions: A Simulation Study of Concentration Effects. *J. Phys. Chem. B* **115,** 14161–14166 (2011).

81. Perin, L. & Gallo, P. Phase Diagram of Aqueous Solutions of LiCl: a Study of Concentration Effects on the Anomalies of Water. *J. Phys. Chem. B* **127,** 4613–4622 (2023).

82. Suzuki, Y. & Mishima, O. Experimentally proven liquid-liquid critical point of dilute glycerol-water solution at 150 K. *J. Chem. Phys.* **141,** 094505 (2014).

83. Biddle, J. W., Holten, V. & Anisimov, M. A. Behavior of supercooled aqueous solutions stemming from hidden liquid–liquid transition in water. *J. Chem. Phys.* **141,** 074504 (2014).

84. Popov, I., Greenbaum (Gutina), A., Sokolov, A. P. & Feldman, Y. The puzzling first-order phase transition in water–glycerol mixtures. *Phys. Chem. Chem. Phys.* **17,** 18063–18071 (2015).

85. Jahn, D. A., Wong, J., Bachler, J., Loerting, T. & Giovambattista, N. Glass polymorphism in glycerol–water mixtures: I. A computer simulation study. *Phys. Chem. Chem. Phys.* **18,** 11042–11057 (2016).

86. Alba-Simionesco, C. *et al.* Interplay of vitrification and ice formation in a cryoprotectant aqueous solution at low temperature. *Proceedings of the National Academy of Sciences* **119,** e2112248119 (2022).

87. Als-Nielsen, J. & McMorrow, D. in *Elements of Modern X-ray Physics* 1st ed., 1–28 (John Wiley & Sons, Ltd, 2011).

88. Als-Nielsen, J. & McMorrow, D. in *Elements of Modern X-ray Physics* 1st ed., 113–146 (John Wiley & Sons, Ltd, 2011).

89. Krogh-Moe, J. A method for converting experimental X-ray intensities to an absolute scale. *Acta Cryst* **9,** 951–953 (1956).

90. Norman, N. The Fourier transform method for normalizing intensities. *Acta Cryst* **10,** 370–373 (1957).

91. Biehl, R. Jscatter, a program for evaluation and analysis of experimental data. *PLoS ONE* **14** (ed Fernandez-Martinez, A.) e0218789 (2019).

92. Kinning, D. J. & Thomas, E. L. Hard-sphere interactions between spherical domains in diblock copolymers. *Macromolecules* **17,** 1712–1718 (1984).

93. Huang, C. *et al.* Increasing correlation length in bulk supercooled H2O, D2O, and NaCl solution determined from small angle x-ray scattering. *J. Chem. Phys.* **133,** 134504 (2010).

94. H. Eugene Stanley. *Introduction to phase transitions and critical phenomena* (Oxford University Press Inc., 1971).

95. Chen, S. H., Lin, T. L. & Kotlarchyk, M. in *Surfactants in Solution: Volume 6* (eds Mittal, K. L. & Bothorel, P.) 1315–1330 (Springer US, 1986).

96. Sheyfer, D. *et al.* Nanoscale Critical Phenomena in a Complex Fluid Studied by X-Ray Photon Correlation Spectroscopy. *Phys. Rev. Lett.* **125,** 125504 (2020).

97. Späh, A. *et al.* Apparent power-law behavior of water's isothermal compressibility and correlation length upon supercooling. *Phys. Chem. Chem. Phys.* **21,** 26–31 (2018).

98. Sengers, J. V. & Shanks, J. G. Experimental Critical-Exponent Values for Fluids. *J Stat Phys* **137,** 857–877 (2009).

99. Nishikawa, K. The Solution Chemistry of Mixing States Probed via Fluctuations: a Direct Description of Inhomogeneity in Mixing. *BCSJ* **94,** 2170–2186 (2021).

100. Berne, B. J. & Pecora, R. *Dynamic Light Scattering: With Applications to Chemistry, Biology, and Physics* 2nd edition (Dover Publications, 2000).

101. DeCaro, C. *et al.* X-ray speckle visibility spectroscopy in the single-photon limit. *J. Synchrotron Rad.* **20,** 332 (2013).

102. A. R. Sandy, Q. Zhang & L. B. Lurio. Hard X-Ray Photon Correlation Spectroscopy Methods for Materials Studies. *Annu. Rev. Mat. Res.* **48,** 167 (2018).

103. Brown, R. G. W., Ridley, K. D. & Rarity, J. G. Characterization of silicon avalanche photodiodes for photon correlation measurements. 1: Passive quenching. *Appl. Opt.* **25,** 4122 (1986).

104. Sutton, M. A review of X-ray intensity fluctuation spectroscopy. *C. R. Phys.* **9,** 657 (2008).

105. H. Voigt and S. Hess. Comparison of the intensity correlation function and the intermediate scattering function of fluids: a molecular dynamics study of the Siegert relation. *Phys. A: Stat. Mech. Appl.* **202,** 145 (1994).

106. Möller, J., Sprung, M., Madsen, A. & Gutt, C. X-ray photon correlation spectroscopy of protein dynamics at nearly diffraction-limited storage rings. *IUCrJ* **6,** 794 (2019).

107. Williams, G. & Watts, D. C. Non-symmetrical dielectric relaxation behaviour arising from a simple empirical decay function. *Trans. Faraday Soc.* **66,** 80 (1970).

108. Alvarez, F., Alegra, A. & Colmenero, J. Relationship between the time-domain Kohlrausch-Williams-Watts and frequency-domain Havriliak-Negami relaxation functions. *Phys. Rev. B* **44,** 7306 (1991).

109. Richert, R. Heterogeneous dynamics in liquids: fluctuations in space and time. *J. Phys.: Condens. Matter* **14,** R703 (2002).

110. Bin, M. *et al.* Coherent X-ray Scattering Reveals Nanoscale Fluctuations in Hydrated Proteins. *J. Phys. Chem. B* **127,** 4922–4930 (2023).

111. Ruta, B. *et al.* Wave-Vector Dependence of the Dynamics in Supercooled Metallic Liquids. *Phys. Rev. Lett.* **125,** 055701 (2020).

112. Caronna, C., Chushkin, Y., Madsen, A. & Cupane, A. Dynamics of Nanoparticles in a Supercooled Liquid. *Phys. Rev. Lett.* **100,** 055702 (2008).

113. Gao, Y., Kim, J. & Helgeson, M. E. Microdynamics and arrest of coarsening during spinodal decomposition in thermoreversible colloidal gels. *Soft Matter* **11,** 6360–6370 (2015).

114. Girelli, A. *et al.* Microscopic Dynamics of Liquid-Liquid Phase Separation and Domain Coarsening in a Protein Solution Revealed by X-Ray Photon Correlation Spectroscopy. *Phys. Rev. Lett.* **126,** 138004 (2021).

115. Bhattacharyya, S. M., Bagchi, B. & Wolynes, P. G. Subquadratic wavenumber dependence of the structural relaxation of supercooled liquid in the crossover regime. *J. Chem. Phys.* **132,** 104503 (2010).

116. Einstein, A. Über die von der molekularkinetischen Theorie der Wärme geforderte Bewegung von in ruhenden Flüssigkeiten suspendierten Teilchen. *Annalen der Physik* **322,** 549 (1905).

117. Shpyrko, O. G. X-ray photon correlation spectroscopy. *J. Synchrotron Rad.* **21,** 1057 (2014).

118. Madsen, A., Fluerasu, A. & Ruta, B. in *Synchrotron Light Sources and Free-Electron Lasers: Accelerator Physics, Instrumentation and Science Applications* (eds Jaeschke, E. J., Khan, S., Schneider, J. R. & Hastings, J. B.) 1617–1641 (Springer International Publishing, 2016).

119. Grübel, G., Madsen, A. & Robert, A. in *Soft Matter Characterization* (eds Borsali, R. & Pecora, R.) 953–995 (Springer Science+Business Media, LLC, 2008).

120. Lehmkühler, F., Roseker, W. & Grübel, G. From Femtoseconds to Hours - Measuring Dynamics over 18 Orders of Magnitude with Coherent X-rays. *Appl. Sci.* **11,** 6179 (2021).

121. Sinha, S. K., Jiang, Z. & Lurio, L. B. X-ray Photon Correlation Spectroscopy Studies of Surfaces and Thin Films. *Adv. Mater.* **26,** 7764–7785 (2014).

122. Zhang, Q., Dufresne, E. M. & Sandy, A. R. Dynamics in hard condensed matter probed by X-ray photon correlation spectroscopy: Present and beyond. *Curr. Opin. Solid State Mater. Sci.* **22,** 202 (2018).

123. Lehmkühler, F. *et al.* Emergence of anomalous dynamics in soft matter probed at the European XFEL. *Proc. Natl. Acad. Sci. U.S.A.* **117,** 24110 (2020).

124. Ruta, B. *et al.* Atomic-Scale Relaxation Dynamics and Aging in a Metallic Glass Probed by X-Ray Photon Correlation Spectroscopy. *Phys. Rev. Lett.* **109,** 165701 (2012).

125. Ju, G. *et al.* Coherent X-ray spectroscopy reveals the persistence of island arrangements during layer-by-layer growth. *Nat. Phys.* **15,** 589 (2019).

126. Shpyrko, O. G. *et al.* Direct measurement of antiferromagnetic domain fluctuations. *Nature* **447,** 68 (2007).

127. Madsen, A., Leheny, R. L., Guo, H., Sprung, M. & Czakkel, O. Beyond simple exponential correlation functions and equilibrium dynamics in x-ray photon correlation spectroscopy. *New J. Phys.* **12,** 055001 (2010).

128. Berkowicz, S. *et al.* Nanofocused x-ray photon correlation spectroscopy. *Phys. Rev. Research* **4,** L032012 (2022).

129. Bikondoa, O. & Carbone, D. X-Ray Photon Correlation Spectroscopy with Coherent Nanobeams: A Numerical Study. *Crystals* **10,** 766 (2020).

130. Johansson, U. *et al.* NanoMAX: the hard X-ray nanoprobe beamline at the MAX IV Laboratory. *J. Synchrotron Rad.* **28,** 1935 (2021).

131. Björling, A. *et al.* Ptychographic characterization of a coherent nanofocused X-ray beam. *Opt. Express* **28,** 5069 (2020).

132. Ghazal, A. *et al.* Recent advances in X-ray compatible microfluidics for applications in soft materials and life sciences. *Lab Chip* **16,** 4263 (2016).

133. Björling, A. *et al.* Three-Dimensional Coherent Bragg Imaging of Rotating Nanoparticles. *Phys. Rev. Lett.* **125,** 246101 (2020).

134. Kawahara, K., Gohara, K., Maehara, Y., Dobashi, T. & Kamimura, O. Beam-divergence deconvolution for diffractive imaging. *Phys. Rev. B* **81,** 081404 (2010).

135. Sasanuma, Y., Law, R. V., Kobayashi, Y. & Sasaki, K. Small-Angle X-ray Scattering Measurements and Image Reconstruction by the Maximum Entropy Method. *Anal. Chem.* **69,** 794 (1997).

136. Aragón, S. R. & Pecora, R. Fluorescence correlation spectroscopy as a probe of molecular dynamics. *J. Chem. Phys.* **64,** 1791 (1976).

137. Evelien J. Nijman, Henk G. Merkus, Jan C. M. Marijnissen, and Brian Scarlett. Simulations and experiments on number fluctuations in photon-correlation spectroscopy at low particle concentrations. *Appl. Opt.* **40,** 4058 (2001).

138. Als-Nielsen, J. & McMorrow, D. in *Elements of Modern X-ray Physics* 1st ed., 29–68 (John Wiley & Sons, Ltd, 2011).

139. Hettel, R. DLSR design and plans: an international overview. *J. Synchrotron Rad.* **21,** 843 (2014).

140. Tavares, P. F., Leemann, S. C., Sjöström, M. & Andersson, Å. The MAX IV storage ring project. *J. Synchrotron Rad.* **21,** 862 (2014).

141. Hallett, J. The Temperature Dependence of the Viscosity of Supercooled Water. *Proceedings of the Physical Society* **82,** 1046–1050 (1963).

142. Collings, A. F. & Bajenov, N. A High Precision Capillary Viscometer and Further Relative Results for the Viscosity of Water. *Metrologia* **19,** 61–66 (1983).

143. Kestin, J., Imaishi, N., Nott, S., Nieuwoudt, J. & Sengers, J. Viscosity of light and heavy water and their mixtures. *Physica A: Statistical Mechanics and its Applications* **134,** 38–58 (1985).

144. Price, W. S., Ide, H. & Arata, Y. *Self-Diffusion of Supercooled Water to 238 K Using PGSE NMR Diffusion Measurements* 1999.

145. Johansson, U., Vogt, U. & Mikkelsen, A. *NanoMAX: a hard x-ray nanoprobe beamline at MAX IV* in *X-Ray Nanoimaging: Instruments and Methods* X-Ray Nanoimaging: Instruments and Methods (ed Lai, B.) **8851** (Proc. of SPIE, 2013), 84.

146. Martensson, N. & Eriksson, M. The saga of MAX IV, the first multi-bend achromat synchrotron light source. *Nucl. Instrum. Methods Phys. Res. A: Accel. Spectrom. Detect. Assoc. Equip.* **907,** 97 (2018).

147. Poikela, T. *et al.* Timepix3: a 65K channel hybrid pixel readout chip with simultaneous ToA/ToT and sparse readout. *JINST* **9,** C05013 (2014).

148. Yousef, H. *et al.* Timepix3 as X-ray detector for time resolved synchrotron experiments. *Nucl. Instrum. Methods Phys. Res. A* **845,** 639 (2017).

149. Skinner, L. B., Benmore, C. J., Neuefeind, J. C. & Parise, J. B. The structure of water around the compressibility minimum. *J. Chem. Phys.* **141,** 214507 (2014).

150. Filianina, M. *et al.* Nanocrystallites Modulate Intermolecular Interactions in Cryoprotected Protein Solutions. *J. Phys. Chem. B* **127,** 6197–6204 (2023).

151. Roseker, W. *et al.* Towards ultrafast dynamics with split-pulse X-ray photon correlation spectroscopy at free electron laser sources. *Nat Commun* **9,** 1704 (2018).

152. Sun, Y. *et al.* Realizing split-pulse x-ray photon correlation spectroscopy to measure ultrafast dynamics in complex matter. *Phys. Rev. Research* **2,** 023099 (2020).

153. Li, H. *et al.* Generation of highly mutually coherent hard-x-ray pulse pairs with an amplitude-splitting delay line. *Phys. Rev. Research* **3,** 043050 (2021).

154. Shinohara, Y. *et al.* Split-pulse X-ray photon correlation spectroscopy with seeded X-rays from X-ray laser to study atomic-level dynamics. *Nat. Commun.* **11,** 1 (2020).